Development of an Experimental and Computational Pipeline for Characterizing the Mechanical Properties and Micromechanical Environment within *In Vitro* 3D Printed Bone Tissue Engineered Scaffolds

Elizabeth Albright Hunt

Thesis submitted to the faculty of the Virginia Polytechnic Institute and State University in partial fulfillment of the requirements for the degree of

Master of Science

In

Biomedical Engineering

Caitlyn Collins, Chair
Raffaella De Vita
Abby Whittington

May 2, 2024
Blacksburg, Virginia

Keywords: dynamic mechanical analysis, computational fluid dynamics, 3D printing, in vitro culture model, fracture healing

Development of an Experimental and Computational Pipeline for Characterizing the Mechanical Properties and Micromechanical Environment within *In Vitro* 3D Printed Bone Tissue Engineered Scaffolds

Elizabeth Albright Hunt

ABSTRACT

Delayed fracture healing is the improper healing of fractures within a reasonable amount of time and is estimated to impact a sixth of all fractures that occur annually in the United States[1]. While blood- and imaging-based bone turnover biomarkers have been thoroughly investigated throughout the healing process of bone, there is still a lack of understanding on how well these biomarkers can predict union in individual patients. Although conventional radiography is the most common clinical practice for assessing bone healing progression, this imaging technique—as well as the other imaging methods used—fails to discern the *in vivo* mechanical environment of bone, and therefore the likeliness of union or nonunion. There is a need to identify mechanical biomarkers that could better differentiate between patients who undergo typical healing progression versus delayed fracture healing. In order to identify these mechanical biomarkers, a 3D *in vitro* cell culture platform that recapitulates the micromechanical environment must be developed and tested. Success of this *in vitro* platform relies on the generation of rigorous testing protocols for assessing stiffness and fluid flow within this organoid system. This study aims to develop an experimental and computational pipeline for mechanically characterizing 3D printed (3DP) scaffolds—Voronoi, IsoTruss, and Truncated Octahedron (TO) geometries—that will be the foundation for future studies to explore patient-specific mechanical biomarkers in these bone tissue engineered scaffolds

A dynamic mechanical analysis (DMA) strain sweep was performed on the scaffolds (n=6 for 4- and 7-day 3T3 fibroblast seeded Voronoi and TO scaffolds, n=4 for 4- and 7-day seeded IsoTruss scaffolds,

n=3 for 4- and 7-day soaked controls for each geometry) to measure storage modulus, loss modulus, and the damping coefficient. The Voronoi geometry increased significantly in storage modulus when seeded for seven days compared to four days ($p=0.0293$). There was also an overall significant decrease in stiffness when the scaffolds were seeded versus non-seeded ($p<<0.001$). Dynamic contrast-enhanced magnetic resonance imaging (DCE-MRI) was performed to produce fluid flow experimental validation data, and this provided insights on the micromechanical environment of the IsoTruss scaffold that were consistent with the computational fluid dynamics (CFD) simulation model. The CFD model was used to calculate wall shear stresses (WSS) for various inlet velocities (0.05, 0.10, 0.15, 0.20, and 0.25 mm/s), with 0.15 mm/s producing WSS best within the range of extracellular matrix formation.

DMA, DCE-MRI, and CFD all confirmed mechanical characteristics of the IsoTruss geometry that were unique to its specific micromechanical architecture. Out of all scaffolds tested, the IsoTruss geometry achieved the maximum (3.47 MPa) and minimum (0.0631 MPa) storage modulus. The computational analysis pipeline revealed that the patterns observed in the DMA experiments could be caused by buckling due to the fourteen-strut intersections and printing infidelity issue related to the IsoTruss geometry. The protocol developed herein for the experimental and computational analyses done on the scaffolds in this thesis will be used in the future on bone organoids to study individualized fracture healing.

Development of an Experimental and Computational Pipeline for Characterizing the Mechanical Properties and Micromechanical Environment within *In Vitro* 3D Printed Bone Tissue Engineered Scaffolds

Elizabeth Albright Hunt

GENERAL AUDIENCE ABSTRACT

Delayed fracture healing and nonunion are prevalent clinical complications with devastating impacts on patient quality of life. The current clinical methods for evaluating bone healing fail to discern the in vivo mechanical environment of bone, and therefore the likeliness of union or nonunion. There is a need to identify mechanical biomarkers that could better differentiate between patients who undergo typical healing progression versus delayed fracture healing. In order to identify these mechanical biomarkers, a 3D in vitro cell culture platform that recapitulates the micromechanical environment must be developed and tested. This study aims to develop an experimental and computational pipeline for mechanically characterizing 3D printed (3DP) scaffolds—Voronoi, IsoTruss, and Truncated Octahedron (TO) geometries— that will be the foundation for future studies to explore fracture healing on an individual, patient-specific level. For experimental characterization, a dynamic mechanical analysis was performed on the scaffolds to measure stiffness and the rate of energy storage and dissipation. Dynamic contrast-enhanced magnetic resonance imaging (DCE-MRI) and a computational fluid dynamics (CFD) simulation were conducted to characterize the internal stresses on the scaffolds and optimize them for bone material generation. DMA testing revealed that the Voronoi geometry increased significantly in storage modulus when seeded for seven days compared to four days. DMA, DCE-MRI, and CFD all confirmed mechanical characteristics of the IsoTruss geometry that were unique to its specific micromechanical architecture.

Acknowledgements

First and foremost I would like to thank Dr. Caitlyn Collins for introducing me to the fabulous world of research. Her passion for bone research inspired me to turn a semester of undergraduate research into a Master's Degree. Thank you for guiding me and supporting me since the beginning.

I would also like to thank my committee members, Dr. Raffaella De Vita and Dr. Abby Whittington, for their time and guidance in helping me complete my thesis. I am inspired by the incredible research that the both of them conduct.

Next, I would like to thank the members of the Bone Organoid team who I had the pleasure of collaborating with over the last couple of years. I also extend my deepest gratitude to Emma and Ed, the undergrads I had the privilege of mentoring who were always willing to learn and help out.

I could not have done any of this without both the academic and personal support from my lab mates and friends. They made coming into work every day a true joy, and I am so thankful for the memories we have made in and outside of the lab.

And finally, I would like to thank my parents and sisters who consistently encourage me. They have always listened to me talk about my research with interest and care, and supported me in ways that no one else can. It is their love and support that mean the most to me.

Contents

List of Tables

List of Figures

Chapter 1

Chapter 2

Chapter 3

Chapter 4

Chapter 1: Introduction

1.1 Introduction and Background

Nonunion or delayed fracture healing is a prevalent clinical complication with a devastating impact on patient quality of life. Bone fracture occurs when applied loading causes the bone to break, and delayed fracture healing is when the fracture does not heal properly or completely within a reasonable timeframe (> 2-3 months). The extreme of delayed fracture healing is called non-union, when boney union fails to occur. These are challenging injuries to treat and lead to significant financial burden and reduced quality of life for the patient[2,3]. An estimated 5 to 10 percent of all fractures that occur each year in the United States exhibit delayed fracture healing, with one sixth of those resulting in nonunion[4]. There are several factors that can contribute to non-union, such as the age, lifestyle, and health of the patient, as well as the location, severity, and type of fracture[3]. As such, identifying patients at risk of delayed fracture healing or nonunion is a significant challenge.

Clinically, bone healing is assessed using medical imaging, typically x-ray or computed tomography, and blood biomarkers that give systemic characterization on bone turnover. Bone-turnover biomarkers such as procollagen type I N-terminal propeptide (PINP), procollagen type I C-terminal propeptide (PICP), osteocalcin, and alkaline phosphate are well-understood to represent bone formation[5]; however, there is not widespread agreement over how these biomarker levels predict nonunion[6]. Several studies indicate how biomarkers predict the individual likelihood of bone fracture, but not bone healing[7]. Given the complexity of bone healing, links to the immune response, levels of trauma, and delay of care have been made to healing outcome[8]. **Existing biomarkers for healing progression and imaging modalities fail to discern which patients experience delayed fracture healing or proceed to nonunion.** Current detection strategies such as radiolucency in planar x-rays and reported

pain by the patients do not account for the *in vivo* mechanical environment[9,10], though studies have also shown a positive relationship between mechanical loading and bone healing[11,12]. Current preclinical models for bone fracture healing rely on 2D cell culture and animal experiments, each with their own limitations regarding translation to patients[13]. 3D tissue culture systems such as organoids and 3D-cell culture models provide an *in vitro* tissue culture platform that allow for the prolonged study of human cells in an environment that mimics conditions in which tissue operates inside of the body[14]. Before addressing this need for a better system to research fracture healing on an individual patient level, *we must first have a method for mechanically evaluating the 3DP scaffolds that will be the basis for the bone organoid.*

1.2 Motivation

The purpose of this study is to develop an experimental and computational pipeline for characterizing patient-specific mechanical biomarkers that indicate individual healing capacity using 3DP bone cell culture models. In order to progress with these 3DP scaffolds as a tool to study fracture healing, we must be able to evaluate their ability to recapitulate healing bone mechanical properties and the bone micromechanical niche. As such, we need an experimental and computational analysis pipeline capable of high-throughput evaluation of the stiffness of full scaffolds as well as the micromechanical stresses within the internal structures induced during static and perfusion culture.

Experimental Pipeline

Dynamic mechanical analysis (DMA) is a method used to characterize the mechanical properties (storage modulus, loss modulus, and damping) of materials through cyclic loading. We do not currently have a procedure in place for testing 3D printed scaffolds, nor have we collected or analyzed preliminary data. These are important measurements because they will tell us how the cell seeding process is impacting scaffold stiffness and enable us to measure changes in scaffold stiffness over time that may be

reflective of extracellular matrix formation (i.e. the formation of osteoid). We will also use the measured storage modulus to compare the stiffness of the scaffolds throughout the seeding and cell culture processes to healing trabecular bone.

Computational Pipeline

The computational side of my thesis is motivated by the need for optimization of our perfusion culture conditions for the scaffolds in future studies utilizing fixed flow rate bioreactors. This system of perfusion cell culture will require decisions to be made on inlet velocity of media that can first be evaluated via computational fluid dynamics (CFD) modeling. Characterization of the micromechanical environment within our target scaffold geometries has not yet been performed. Using CFD modeling, our goal is to compare the internal stresses acting on the structure at different flow rates to known stresses that encourage the development of extracellular matrix in other *in vitro* studies. Through this computational pipeline we will have a way of mapping the velocity and direction of fluid flow to calculate wall shear stresses and inform perfusion bioreactor decisions. Before performing long term perfusion culture with human cells, it is important to understand the micromechanical environment of our target scaffold geometries under review.

As previously discussed, the larger societal issue of delayed fracture healing and nonunion are significant medical problems. By creating an experimental and computational pipeline for evaluating 3DP bone organoid structure and micromechanical environment within a perfusion bioreactor system, future studies can be performed using patient primary cells to better understand non-union progression and improve treatment plans in human patients. I am highly motivated by the potential for this research to allow for the further study of mechano-regulation in fracture healing.

1.3 Introduction of Aims and Hypothesis

1.3.1 Aim 1

My first aim is to characterize cell proliferation and progression of extracellular matrix (ECM) formation and maturation using dynamic mechanical analysis (DMA).

Hypothesis: Pore size, microarchitecture of 3DP bone scaffolds, and days seeded will mediate mechanical properties determined via DMA.

Approaches and Outcomes: The three scaffold geometries (Fig 1.1, 10mm x 10mm x 10mm), Truncated Octahedron (TO), IsoTruss, and Voronoi, will be 3D printed using vat photopolymerization and a novel 50 wt% epoxidized soybean oil acrylate (ESOA) and 50 wt% PEGDA photopolymer resin (provided by a collaborator in Materials Science Engineering/Chemical Engineering at Virginia Tech). The scaffolds will be seeded with immortalized murine fibroblast cells (MC3T3-E1,$1x10^5$ cells/scaffold) and cultured for 4 and 7 days under static conditions. Confocal microscopy will be used to confirm successful cell adhesion and proliferation and to analyze cell distribution. DMA testing in compression will be performed, including a strain sweep at a frequency of 0.1 Hz starting with a dynamic amplitude (DA) of 0.2 mm (4% strain) and increasing by 0.1 mm until reaching 1 mm DA (10% strain). Storage modulus, loss modulus, and tan(delta) will be recorded. The storage modulus data will be important in determining how pore size and microarchitecture impacts scaffold elastic mechanical properties, which is expected to increase with culture time. Assessments about print fidelity can also be drawn from this data. From this study, we will develop robust mechanical testing and imaging protocols and determine the optimal geometry for recreating the bone microenvironment.

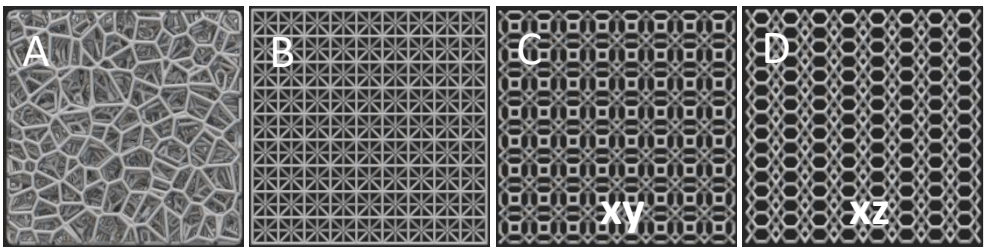

Figure 1.1: Ideal CAD geometries. A) Voronoi, B) IsoTruss, and C-D) TO structures are printed by Dr. Whittington's lab.

1.3.2 Aim 2

My second aim is to develop a validated computational model to simulate fluid flow and optimize wall shear stress (WSS) within the 3D printed scaffolds.

Hypothesis: Testing a range of inlet velocity flow rates will produce WSS in the range of ECM formation, allowing for the optimal rate to be chosen for future perfusion systems.

Approaches and Outcomes: Computational Fluid Dynamics (CFD) modeling will be used to perform a virtual fluid shear test on idealized computer automated design (CAD) geometric models of the scaffolds, simulating 3D culture conditions (COMSOL). This analysis will reveal how variations in pore distribution, pore size, and fluid flow impact the biomechanical properties of the different geometries, with peak WSS and WSS distribution as our metric of interest as they are tied to ECM mineralization in bone cell-seeded 3D scaffolds[15,16]. The CFD analysis will be validated against dynamic contrast-enhanced magnetic resonance imaging (DCE-MRI) data, which can be used to measure the vector field of fluid flow velocity within the scaffolds[17]. Here, scaffolds will be modified to fit in a 12 mm diameter transwell insert, maintaining the same internal structures as in Aim 1. CFD model optimization will be performed until the shear velocities achieve a wall shear stresses on the order of extracellular matrix formation, and the resulting velocity magnitude and direction fields will be compared to the results of the DCE-MRI analysis. Through this simulation, the inlet velocity for perfusion cell culture of the scaffolds will be optimized.

Chapter 2: Literature Review

The following literature review was conducted to better understand the researched principles related to bone biomechanics pertaining to my thesis. Specifically, I investigated literature to complete my understanding of the physiological and mechanical properties of bone, fracture healing, clinical prevalence and assessment of fracture healing, alternative methods for assessing fracture healing, and bone organoids.

2.1 Physiological and Mechanical Properties of Bone

Bone is a major component of the human musculoskeletal system, and serves the human body with several functions vital to life. Before conducting any research on bone biomechanics, it is important to first understand the micromechanical environment of human bone. Bone serves several functions to human beings: it protects organs, provides structure for the body, facilitates movement through locomotor functions, and serves as a reservoir for vital nutrients[18–20]. There are two major tissue-level components, namely cortical and trabecular bone.

Cortical bone makes up about 80% of adult bone, and serves as a structural material that encapsulates and protects the bone marrow space due to its denser composition[19] (i.e. low porosity, ~ 2 to 10%[21]). Since cortical bone forms the outer shell of individual bones, there are two surfaces that make up the cortical bone compartment—the periosteal and endosteal surfaces. The outer periosteal surface plays an important role in repairing fractures in bone's surface[18], and will become important later when discussing the fracture healing process. The periosteum is further broken up into two surfaces: a fibrous outer layer and the inner cambium, or cellular, layer[22]. Osteoprogenitor cells are located in the cambium layer, which are important in the formation of new bone[22]. The endosteum, although not distinguishable using an electron or light microscope, is where bone marrow and bone surface meet[22]. At the microstructural level, osteons in cortical bone is made up of layers of mineralized tissue (interstitial

lamellae) and osteons (concentric lamellae). The osteons make up the Haversian system, which form cylinders with a 200 mm diameter and 400 mm height[18]. There are generally 5 to 15 lamellae that orient concentrically to form a Haversian system[22]. At the center of the Haversian system, is a blood vessel, which is important in supplying bone with a large portion of the body's cardiac output (about 10 to 20 percent)[22]. The structure of cortical bone is represented in Figure 2.1.

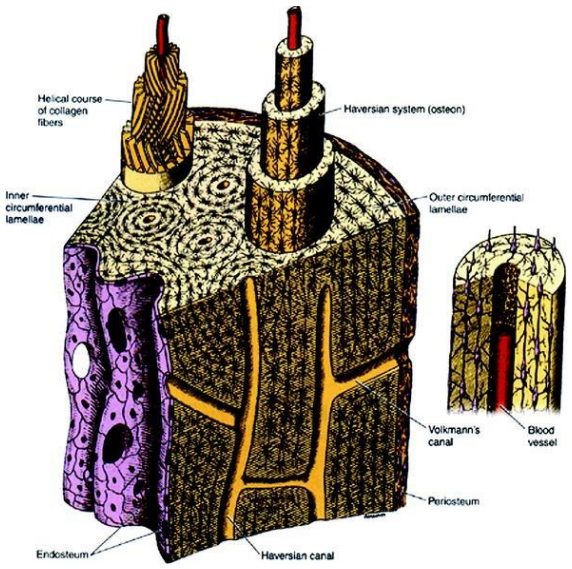

Figure 2.1: Schematic showing a section of cortical bone and Haversian system (adapted from [5]).

The remaining 20% is composed of trabecular, also called cancellous, bone. Much more porous than cortical bone (high porosity, average of 79.3%[23]), trabecular bone has a spongy composition, as seen in Figure 2.2, and is located within the cortical shell at the ends of long bones and is also on the inside of irregular and flat bones[24]. Trabecular bone is much more active metabolically because there is less mineralization and more surface area than in cortical bone[19]. Plates and rods make up trabecular bone microstructure, which have an average thickness ranging from 50 to 400 mm[18], and pores that are around 1 mm thick[24]. The plates and rods are arranged in a pattern that gives this bone compartment a spongy look. Human bones vary in the proportion of trabecular and cortical bone composition due largely in part to the physiological loading demands at different anatomical locations—there is relatively

more trabecular bone found in vertebrae rather than long bones where the cortices are thick, for example[19]. These intricate characteristics of trabecular bone are challenging to model, but their role in the function of bone make it critical to accurately model this architecture.

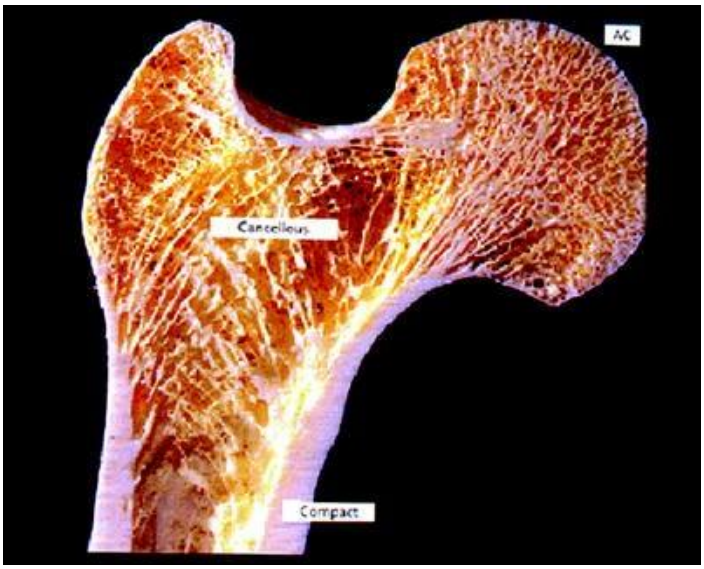

Figure 2.2: Cross section of human long bone (adapted from [5]).

In both cortical and trabecular bone, collagen fibers, hydroxyapatite mineral crystals, non-collagenous proteins, and water make up the basic building blocks of the tissue. The alternating orientation of collagen fibers in adjacent lamellar layers in adult bone increases bone's strength[19]. In immature or newly formed bone, collagen fibers are arranged in a random pattern called woven bone, which is not as strong as lamellar bone[18,22]. Woven bone is associated with growth and bone healing, and is therefore found in areas of the skeleton where remodeling is occurring[22].

The smaller scale composition of bone is also important to understanding its mechanics. Bone is mostly made of mineral, at about 50 to 70%, followed by organic matrix (20-40%), water (5-10%), and lastly lipids (less than 3%)[18]. Most of the 50-70% that is mineral is calcium hydroxyapatite (Figure 2.3)[18,19]. Type I collagen fibers (Figure 2.3) make up the organic matrix, which includes proteoglycans, glycoproteins, phospholipids, phosphoproteins, and g-carboxylated proteins[18,22]. The mineral and

collagen matrix provide bone with two important structural qualities: stiffness and toughness, respectively[19].

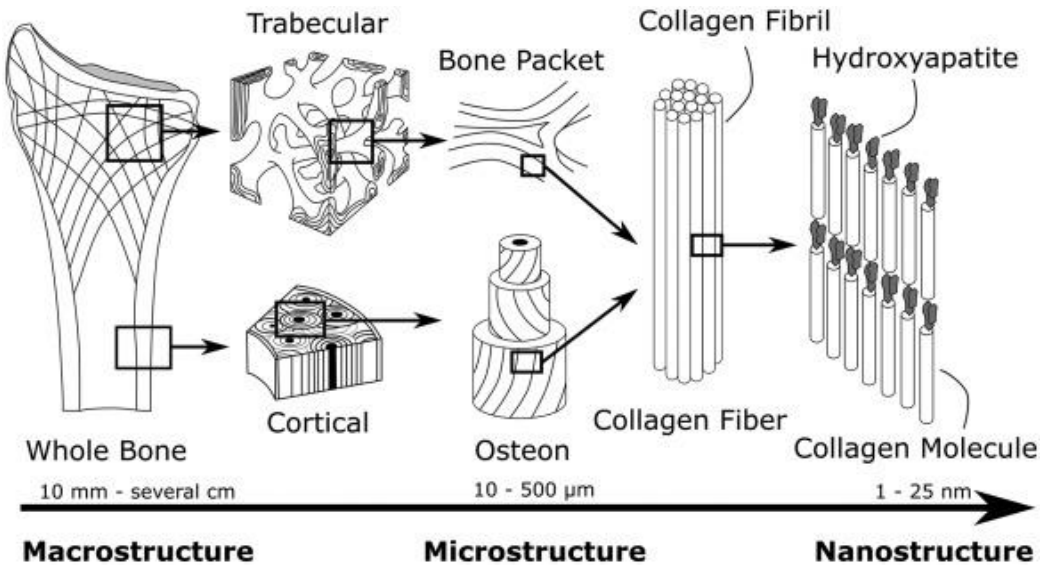

Figure 2.3: Organization of bone from whole bone to hydroxyapatite and collagen molecules (adapted from [4])

When discussing the mechanical properties and values of bone, I will focus on trabecular bone because that is the type of bone that we will be modeling using 3DP porous scaffolds in this thesis. There are many factors that impact the mechanical properties of trabecular bone, such as the anatomical location of the bone and the age and health of the subject[24]. Because of this, trabecular bone is largely heterogeneous in terms of mechanical properties. Figure 2.4, adapted from Keaveny et al., captures the range in elastic moduli within the human tibia. This heterogeneity directly impacts the interpretation of data collected from our 3DP scaffolds, as one geometry could be a better model for trabecular bone from one anatomical site than another.

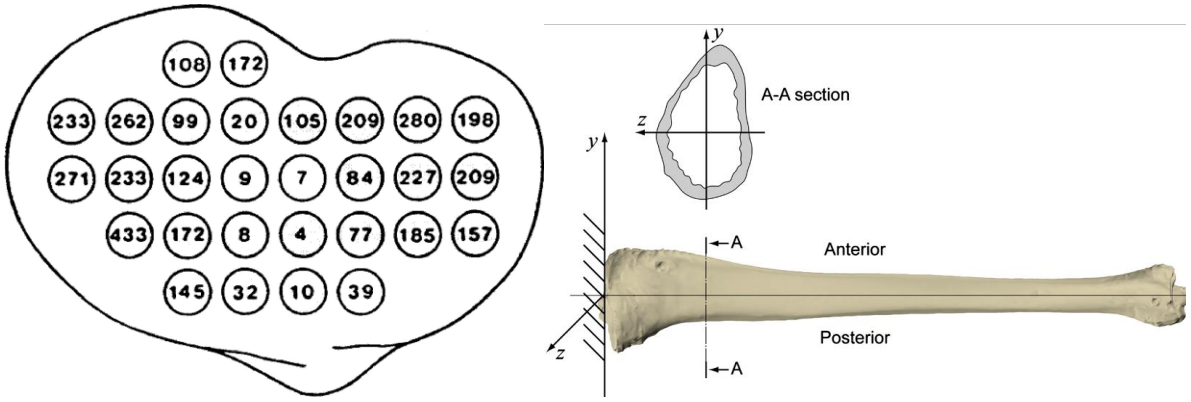

Figure 2.4: Left: cross section of human tibia with compressive elastic moduli (MPa) values labeled at various regions (adapted from [7]). Right: For reference to the calculations in the left, a human tibia from Cristofolini et al. shows the same cross section from the proximal end of the tibia[25] *(adapted from [8]).*

Although there is a wide range of elastic moduli measurements just within the tibia cross section (4 to 433 MPa), there is even greater variation across the entire skeleton. Studies have quantified these variations across the skeleton by age[26], direction (vertical versus horizontal)[26], and anatomical location[27]. This dramatic variation in stiffness from one location of the skeleton to another demonstrates how important the role of anatomical site plays in the biomechanical properties of bone. The principle that guides this pattern is Wolff's Law, which in simple terms states that bone grows where it is needed and decreases where it is not. For trabecular bone, the microarchitecture reorganizes in order to perform best mechanically as a result of the loading it experiences[28]. Aside from anatomical site, age also plays a large role in trabecular bone biomechanics. Within the spine, after about 20 years old, there is an 11 percent decrease in ultimate trabecular stress each 10 years[24] which is associated with a loss in bone density. Trabecular bone in the spine loses almost half of its density from 20 years to 80 years old[26]. Another mechanical characteristic of bone that has an impact on the geometry is the anisotropic nature of modulus[24]. This means that the modulus of trabecular bone changes depending on the direction in which it is tested. All of these properties become critical in the design and evaluation of bone models that aim to recapitulate the micromechanical structure of bone. Bone is not a specific enough structure

to model—the location, orientation, porosity, condition, and several other factors of bone must be considered for the model.

2.2 Fracture Healing

A significant application of the research I am conducting for this thesis is in the assessment of strain mediated fracture healing. Specifically, the identification of mechanical biomarkers that could potentially indicate proper healing of fractured bone. Bone fracture can be defined as a stress-induced break in bone tissue[13]. Fracture healing, or union, is when the original mechanical stiffness and strength are restored to the bone[29]. Understanding the process that bone undergoes when repair is necessary is vital in order to investigate potential indicators of nonunion. The healing process of bone (Figure 2.5) can be broken down into four separate phases: the inflammatory response, soft callus formation, ossification, and remodeling[30].

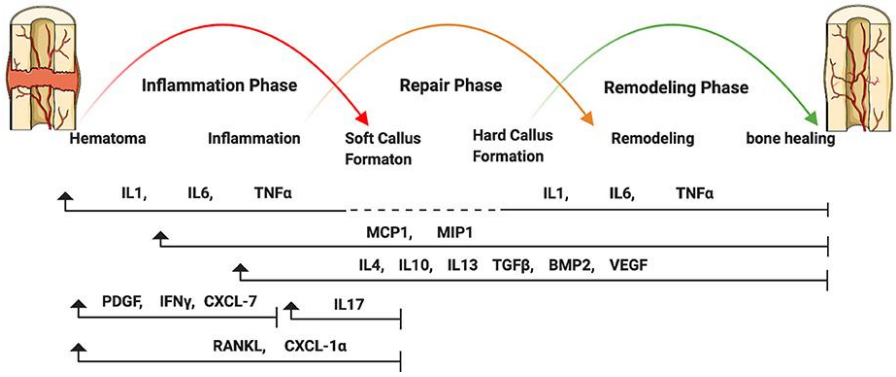

Figure 2.5: Schematic summary of the four fracture healing phases (adapted from [15])

The inflammatory response is the body's first step in recognizing and beginning to repair damaged induced in fractured bone tissue, and plays a critical role in determining how the rest of the healing process progresses[31]. Within the inflammatory phase, the main actions that are accomplished are granulation tissue and hematoma formation and the recruitment of cells and cytokines needed to initiate repairs[32,33]. As a result of the stress on the bone tissue (i.e. mechanical stimulus), cytokines such as interleukins-6 (IL-1), interleukins-6 (IL-6), and tumor necrosis factor (TNF-α) signal for the beginning of

the repair process[31,33]. These cytokines initiate the recruitment of mesenchymal stem cells which differentiate into the cells that will ultimately form bone—osteoblasts[33]. Polymorphonuclear neutrophils (PMNs) and bone-specific macrophages, called osteomacs, are part of the inflammatory response and facilitate homeostasis by eliminating debris and dead cells from the fracture area[31]. The soft callus that forms in this stage is predominantly cartilaginous tissue that grows around the bone, stabilizing the fracture and connecting the broken segments of bone[34,35]. This soft callus will ultimately be mineralized and transformed into new bone material through a process called ossification[36] . There are two ways that this ossification occurs: endochondral and intramembranous ossification[31,16]. Inside of the fracture gap or space between bone fragments, the cartilaginous callus that was just formed transforms into mature bone via endochondral ossification[16]; here, the cartilaginous callus is slowly replaced by unorganized mineralized tissue (i.e. woven bone). In contrast, the direct formation of hard callus at the fracture site occurs during intramembranous ossification, in which osteoblasts are differentiated from osteoprogenitor cells and begin to produce osteoid (unmineralized extracellular matrix) that quickly transforms into woven bone[31]. Finally, in both cases, the woven bone formed during ossification is remodeled into lamellar bone during the remodeling phase[37]. This complex process makes it difficult to assess bone fracture healing dynamics *in vivo,* and to differentiate at which stages certain mechanical properties can be observed.

Delayed Fracture Healing

Although there is variance on the time frames in which the four stages of bone healing can occur, the process usually takes about a month and a half to two months for long bone fractures to heal[38]. Delayed fracture healing occurs when the bone does not heal within the standard amount of time, however this time frame can vary by anatomical location, surgical procedure, and even be adjusted based on patient age or the presence of comorbidities. The US FDA defines nonunion as nine months

after injury in which the fracture has not healed or three stagnant months with no indications of progression towards healing[38].

2.3 Clinical Prevalence and Assessment of Fracture Healing

Clinical Prevalence

Improper fracture healing, or delayed fracture healing, can lead to nonunion and is a serious prevalent clinical complication with a significant impact on quality of life. These are challenging injuries to treat and lead to significant financial burden and reduced quality of life for the patient[2,3]. Among the lifetime costs related to injuries, fractures make up the largest portion of the costs at 24 percent[39]. In the United States, six million fractures are estimated to occur annually, and about 5 to 10 percent of all fractures that occur each year in the United States experience delayed fracture healing. One sixth of cases experiencing delayed fracture healing will progress to nonunion (approximately 50,000-100,000 cases)[4]. There are several factors that can contribute to non-union, such as the age, lifestyle, medications, and health of the patient, as well as the location, severity, and type of fracture[3] . Although bone mass decreases as adults age, in the United Kingdom, 35 to 44 year olds experience the peak incidence for nonunion [40]. There are several methods that clinicians use to evaluate the progression of these fractures in patients, with varying equipment (Figure 2.6) and professional opinions on best ways to come to clinical diagnoses.

Figure 2.6: Example equipment of conventional x-ray[41], ultrasound[42], and computed tomography[43].

Conventional Radiography

Radiography is a qualitative analysis and is the most commonly used method of clinically evaluating fracture healing. The metrics that radiography is able to capture are cortical bridging, trabecular crossing, fracture line loss, and formation of callus tissue[39]. These metrics are calculated by observing how callus tissue has formed at the location of the fracture by tracking changes in radiolucency or brightness of the bone tissue[44]. Although this method is affordable and accessible, there are concerns with how well the qualitative data correlates to healing and mechanical strength of the bone[39, 44]. Research shows that of all metrics taken in radiography, cortical bridging most accurately depicts what is happening mechanically[39].

Despite this, there is no established "gold standard" for assessing the healing progression of bone fracture[39,45,46]. Further, it is possible that there are discrepancies between clinical standards for evaluating fracture healing (radiograph) and micromechanical standards for evaluating fracture healing[39]. For example, the information that a radiograph tells us about the state of a fracture could disagree with what is happening on a histological level in the patient's bone. Additionally, there are inconsistencies with how physicians define the nonunion timeline[39,45]. In a study conducted by Bhandari et al. (2002), 444 orthopedic surgeons from around the world participated who specialized in trauma were polled, and a range of 1 to 8 months was utilized to classify delayed fracture healing. This range was 2 to 12 months for nonunion[45].

To complicate clinical diagnosis, a single radiograph might not capture the patient's progress in healing, or bone strength. As such, multiple radiographs of the same fracture taken at different time points gives physicians a better idea of bone strength. Panjabi et al. (1989) present supporting evidence for this concept in their study in which physicians were presented with one set of radiographs versus two sets of radiographs. The physicians tended to under-evaluate the healing progression of the fracture

when given one set of radiographs; however, the physicians more accurately evaluated the relative progression of healing when there were two sets to compare[47]. Note, radiographs alone do not provide ample information for assessing bone healing. Further, the use of radiography in evaluating fracture healing is further complicated by the widespread variation among fracture pattern, location of fracture, and the patient[29].

Patient Self-Evaluation

Although not a type of sophisticated imaging technique, a very important factor in the evaluation of fracture healing is symptoms of pain at the fracture site for the patient. Physicians perform evaluations on patients that include palpations to determine tenderness and will ask for reports of pain at each visit[48]. In a study conducted by Morshed et al. (2008), pain in weightbearing and pain during palpitation were the two most commonly used criteria during clinical examinations to determine fracture healing[39]. There are limitations, however, to this evaluation of healing. Often times, pain can be independent from whether or not the fracture is healed. Pain in a completely healed fracture of the tibial shaft can persist for about three years after the fracture[49]. Additionally, all patients are different and can either have trouble expressing the degree of their pain or be more sensitive to the pain than other patients. This is a useful tool to be used in combination with other imaging techniques and is not used alone to determine healing status.

Ultrasound

Ultrasound is a method of fracture healing evaluation that has recently grown in popularity[44]. Ultrasound uses high-frequency waves produced through tissue in order to create images of the tissue being analyzed[44,50]. Its main benefit, compared to conventional radiography, is that ultrasound can detect callus formation much earlier, which reflects the potential for ultrasound to be used as an indicator of nonunion[40,51].

In a study conducted by Ricciardi et al. (1993), they found that there is a significant correlation between healing progress of bone based on calcification in the periosteal apposition and the intensity in which the ultrasound waves are echoed[50]. Furthermore, they were able to detect callus formation via ultrasound before radiographs demonstrated any indication of callus formation activity. For example, Moed et al. (1998) were able to use ultrasound to determine fracture healing, or union, at an average of only 6.5 weeks compared to the average 19 weeks it takes to determine with radiography[51]. While this correlation establishes an important link between ultrasound imaging and healing status ultrasound could not quantitatively characterize healing mechanics alone[50].

Unlike other imaging sources that use ionizing radiation, ultrasound does not image through cortical bone[52]. As such, ultrasound imaging tracks changes in external hematoma and callus formation. The hematoma caused by a fracture shows up dark on an ultrasound because it is hypoechogenic. During calcification, the region begins to produce a heavily contrasted boundary that is clear via ultrasound[52]. These changes in echogenicity take place before bridging callus forms and leads to the mineralization that can be seen later on radiographs.

While ultrasound has significant benefits to detecting union early on in the healing process, there are limitations to the images produced by ultrasound. Hard tissue that develops during fracture healing cannot be visualized very efficiently using ultrasound[52]. There is also a certain level of skill required to operate ultrasound equipment, making it heavily dependent on the technician conducting the imaging[52].

Computed Tomography

Computed tomography (CT) is most beneficial in its ability to reconstruct 3D images of the scanned region for quantitative analysis[39]. Through these 3D reconstructions, bone density and volume

of callus tissue can be measured to provide insights on stiffness and strength in torsional loading of long bones[39,53]. Boer et al. (1998) was able to use this callus density and subsequent measurements acquired through CT to predict the level of fracture consolidation[53]. Figure 2.7 depicts a series of scans and reconstructions of a tibial fracture, four weeks from the incident.

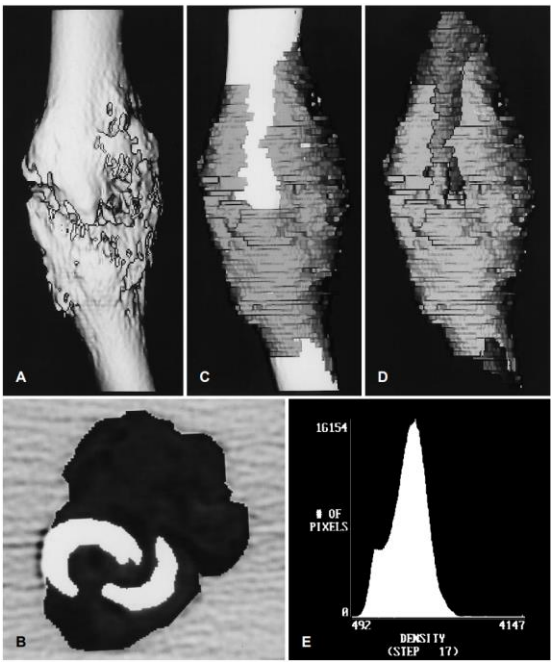

Figure 2.7: From den Boer et al., this is an example of a 3D reconstruction of a tibial fracture using CT. A) the CT reconstruction in 3D view; B) the center cross-section of the fracture in which the callus has been segmented (black); C and D) the same reconstruction with the callus segmented (gray) with (C) and without (D) the bone. E) the pixel density frequency distribution (adapted from [41]).

Furthermore, Bhattacharyya et al. (2006) found that CT was very accurate in diagnosing union and nonunion. For 35 patients, CT had an accuracy of 89.9% in detecting nonunion; however, the specificity was lower at 62%[49]. In this study, physicians using CT occasionally declared a fracture that was healed as a nonunion (3 instances), but CT was overall very useful to confirm fracture healing[49]. The low specificity of CT imaging is one of the most significant limitations of CT in evaluating nonunion.

Blood Testing

Research has also been done on the role of blood testing to evaluate fracture healing. Deficiencies in calcium and vitamin D can contribute to delayed fracture healing, and after fracture-causing injuries the skeleton can undergo calcium mobilization in non-fractured bones in response to such deficiencies[36]. Calcium plays an important role in bone health in that it is an important mineral that contributes to the strength of bones, while also regulating levels of blood calcium[36]. Vitamin D contributes as a regulator of calcium levels, which plays important roles in bone reabsorption and remodeling[36]. As both of these are important factors in fracture healing, they can be tested to give physicians an idea of the response the body undergoes to heal a fracture. Unfortunately, this lacks specificity to the fractured region and alone cannot be used to indicate progression to healing. Another study conducted by D'Amelio et al. (2010) analyzed the levels of osteoblasts precursors, osteoclast precursors, bone formation markers, TGFβ1, and PTH immediately after fracture and then about two weeks after fracture[54]. They found that the osteoblast and osteoclast precursor levels did not change in the blood while the fracture was healing, but there was an increase in TGFβ1[54]. TGFβ1 is a growth factor that stimulates the increase of osteoblast precursors, and additional study of how TGFβ1 correlates to progression of healing could reveal significant insights on evaluating union and nonunion[54].

2.5 Alternative Methods for Assessing Fracture Healing

Animal models

When physiologic behavior of animals match that of humans, animal models can be extremely useful in better understanding human anatomy or conducting research before using human tissue. Considering the limitations of clinical imaging in predicting non-union, we look to practices that researchers use to improve these systems. For nonunion, specifically, small ruminants (sheep and goats), rabbits, rats, and mice are commonly used to study healing progression[55]. The repair rate of bone for small ruminants is on a more relevant scale to humans, taking about 32 weeks to one year[55]. While this is

beneficial in that it mimics human behavior, a rat with a shorter repair time could be better suited to a lab-based study constrained by time[55]. There are many factors to consider when choosing an animal model that best fits a particular study. Gao et al. (2023) surveyed the animal models used to study fracture healing and concluded that about 53.5 percent of models use mice[37] (Figure 2.8). Note that fracture studies include research not only on fracture healing but also on fracture mechanics and bone strength. Gao et al. cite mouse, canine, and non-human primates as three species that have commonly been used to study nonunion and fracture healing.

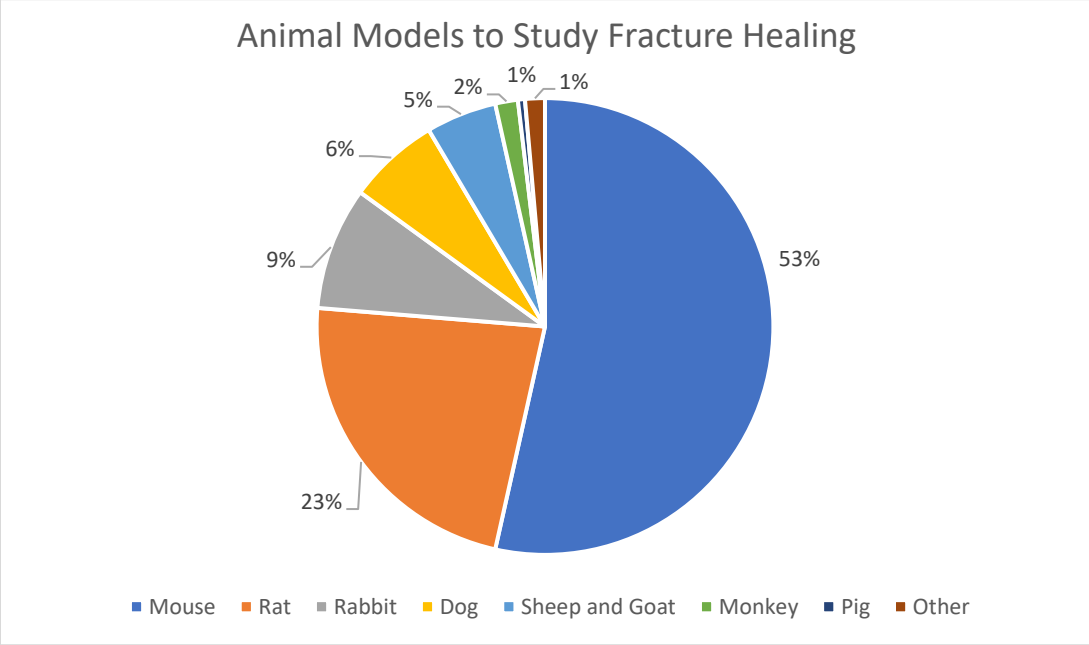

Figure 2.8: Break down of animal species that are used in fracture-related research studies (adapted from [22]).

Limitations of Animal Models

While models for fracture healing have been studied for mice[56–58], rats[59], rabbits[60], canines[61–65], and non-human primates[66,67], there are several limitations to these models when studying the micromechanical environment of bone. A limitation to using animal models to study fracture healing and nonunion is that, while they can model certain factors that might encourage nonunion, they cannot be

fully patient-specific models. They reveal principles of bone healing that are generally applicable to humans, but a single model does not take into account the individual factors that influence healing progression. Additionally, the fractures in most of these models are not naturally-occurring and must be induced in the animal. While they are useful in studying physiological bone healing, they lack a predictive aspect to nonunion research. *In vivo* animal models are also limited in that many components of the bone metabolism process are dependent on the species[13,68]. This means that some animal models do not translate well to humans. The environmental conditions of animals versus humans is another important factor with regards to fracture healing[68]. Mechanical stimulus plays a significant role in the bone repair, and the musculoskeletal differences between animals (quadrupeds) and humans (bipeds) directly impacts these mechanical forces that their skeletons take on. In consideration of these limitations, as well as ethical factors, better models using cell culture systems should be explored.

Cell culture

Cell culture systems allow for the prolonged study of cells in an environment that is consistent with the goals of the research. 3D *in vitro* cell culture systems have been developed to study how bone forms and ossifies via established cell lines as well as using patient primary cells[69]. Cell cultures of human bone cells are able to mineralize into extracellular matrix (ECM) when maintained with β-glycerol phosphate, calcium, and ascorbic acid[70]. Along with ECM formation, Robey and Termine (1985) also found that type I collagen and osteonectin were biosynthetically produced in the culture[70]. This study was conducted early on in the development of 3D bone cell culture systems and provided much promise on bone cell metabolism research. Additionally, by using human bone cells for culture, the individual, patient-specific aspect of 3D culture systems was highlighted. While 2D cultures are limited in the fact that they cannot recapitulate the microenvironment of human bone; Figure 2.9 summarizes the pros and cons of 2D and 3D cell culture systems in bone healing research (created by Ehnert et al)[68]. They

identified one of the most important limitations of existing *in vitro* models, which is that it is difficult, if not impossible, to exert mechanical stimulus. A solution to the lack of rigidity for mechanical stimulus in 3D culture systems is the integration of a structural component to the culture (i.e. 3D culture or organoid) that mimics the organization of bone.

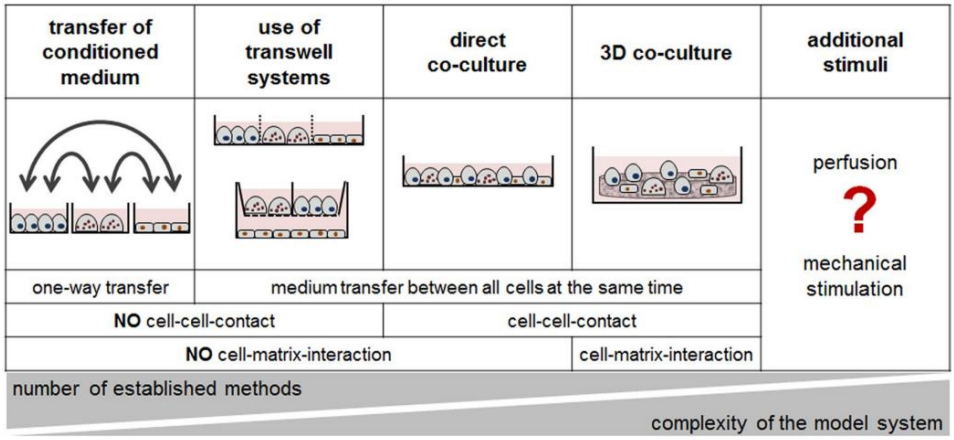

Figure 2.9: Compilation of pros and cons of 2D in vitro cell culture systems for studying fracture healing (adapted from [56])

2.6 Organoids

Organoid Composition

Organoids provide an *in vitro* tissue culture platform that allow for the prolonged study of human cells in an environment that mimics *in vivo*[14]. To some degree, organoids must replicate the structure and function of the tissue being analyzed[71]. The use of organoids to research human tissue is fairly recent, with the first organoid developed in 2009[13]. Currently there are several different structural components that have been explored in order to provide the 3D culture systems with a surface in which bone cells can grow on. Iordachescu et al. (2021), for instance, seeded osteoblasts and osteoclasts onto micro-trabeculae from a femoral head[72]. Ceramic materials have also been used as scaffold materials: Papadimitropoulos et al. (2011) synthesized porous, cylindrical structures from hydroxyapatite/beta-tricalcium phosphate[73]. They found that when co-cultured with stromal vascular fraction and CD14+ cells, there was osteoclast activity and matrix deposition[73]. Park et al. (2021) developed a novel

structural material that they call demineralized bone paper (DBP)[74]. This DBP is composed of cortical bone that has been demineralized and cut into thin slices and unmineralized bone extracellular matrix[74]. Silk fibroin is another common material for biocompatible scaffolds[75,76]. Beyond material selection, researchers have taken several different approaches to create structural components on which to seed bone cells in order to replicate the micromechanical environment of human bone.

Organoid Design Considerations

From a geometric perspective, trabecular bone porosity, permeability, surface morphology, as well as strut thickness, size, and shape must be accounted for[77]. For example, the ceramic scaffolds mentioned above created by Papadimitropoulos et al. were solid cylinders with 80% porosity, a height of 4 mm, and diameter of 8 mm[73]. However, controlling for porosity only captures a small portion of the complexity of trabecular bone morphology. Several fabrication methods have been used to produce scaffolds, such as solid free-form,[75] electro-spinning,[78] and 3D fiber deposition[77,79]. All of these factors must balance the biological environment it is creating for cells with the mechanical architecture that the material and design allows[75]. These design choices about porosity, morphology, size, fabrication, etc. are important because they determine the environment in which the cells being seeded into the scaffolds will grow. The process in which cells differentiate is greatly affected by the topological and biochemical environment[77]. This is another factor that makes 2D culture systems unsuitable for mimicking the complex bone matrix.

In a study on design considerations for scaffold design, Hollister (2005) illustrates the impact of pore shape and volume fraction on the mechanical properties and permeability of a bone scaffold (Figure 2.10). With greater volume fraction, the modulus of the scaffold increases and the permeability decreases[75]. These properties of a unit cell can be applied across larger-scale scaffold design to maximize

characteristics that are important in a particular study. In a study conducted by Moroni et al. (2006), a scaffold with pores of differing size and shape were tested via dynamic mechanical analysis (DMA). DMA testing demonstrated a decrease in dynamic stiffness and increase in tan delta, a measure of viscous damping, as the porosity of the tested scaffolds increased[79]. Porosities from 28.9% to 91.2% were tested, with the storage moduli ranging from an average of 13.7 MPa to 0.262 MPa, respectively[79]. This agrees with Hollister's analysis that the more scaffold there is relative to pore space, the stiffer the material gets. DMA is a useful tool in analyzing organoids because it can be modified to fit physiological conditions of the particular tissue being tested[79]. Rather than a force-to-failure mechanical test, a DMA test allows for repetitious movement that simulates motion such as walking where there is loading and unloading.

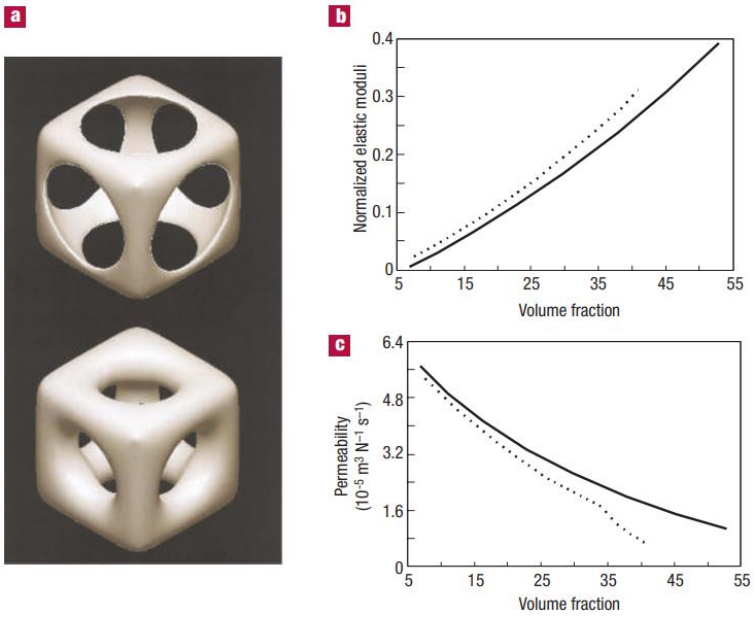

Figure 2.10: Impact of pore shape and volume fraction on elastic modulus and permeability of representative unit cells. The dotted lines in B and C represent the sphere-shaped pore, and the solid lines represent the cylinder-shaped pore (adapted from [64]).

Another mechanical stimulus that can be applied to scaffold can originate from the flow of solution through the scaffold to form wall shear stresses (WSS). The most common way to induce these

stresses is by using a perfusion bioreactor system in which solution is cycled through the scaffold at a controlled rate. Vetsch et al. (2017), studied the WSS required for osteogenic differentiation by applying two flow rates (0.001 m/s and 0.061 m/s) to silk fibroin scaffolds[15]. They found that the smaller flow rate promoted early stages of fracture healing; whereas the faster rate produced WSS at 0.55 to 24 mPa and promoted osteogenic differentiation and the formation of ECM[15]. Similarly, Zhao et al. (2019) analyzed the WSS produced on a silk fibroin scaffold at an inlet velocity of 0.0005 m/s, and were able to achieve WSS on the order of ECM formation[76]. Figure 2.11.11 shows Zhao et al.'s simulation of WSS on the surface of the scaffold at different fluid velocities. As a result of their simulations, they were able to determine the percentage of surface area in which the scaffolds underwent a WSS in the range required to induce mineralization[76]. This figure serves as an excellent visual representation of the force that fluid flow can produce in the micromechanical environment of an organoid. These forces have significant implications on osteogenic differentiation and, therefore, will have a major impact on the success of a scaffold in mimicking the micromechanical environment of bone.

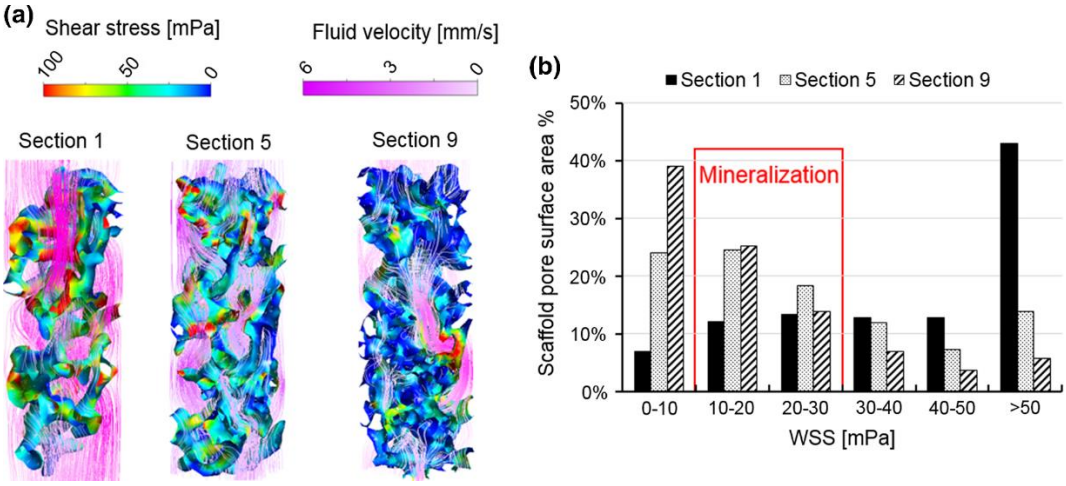

Figure 2.11: WSS and fluid velocities that induce mineralization in silk fibroin scaffolds (adapted from [65])

The organoid models mentioned in this section demonstrate the complex requirements to mimic the structure of trabecular bone *in vitro.* Bone is a constantly changing tissue that requires specific

architecture and mechanical stimulation to function properly. This literature review captures the deep complexities of bone and fracture healing as well as the challenges researchers face in developing models in which bone can be robustly studied.

References

1. Buza JA, Einhorn T. Bone healing in 2016. Clin Cases Miner Bone Metab. 2016;13(2):101-105. Accessed February 14, 2024. https://eds.p.ebscohost.com/eds/pdfviewer/pdfviewer?vid=0&sid=5f1ef49d-ee47-489c-a3b1-8d812580d7e8%40redis
2. Hak DJ, Fitzpatrick D, Bishop JA, et al. Delayed union and nonunions: Epidemiology, clinical issues, and financial aspects. Injury. 2014;45(SUPPL. 2):S3-S7. doi:10.1016/J.INJURY.2014.04.002
3. Schlundt C, Bucher CH, Tsitsilonis S, Schell H, Duda GN, Schmidt-Bleek K. Clinical and Research Approaches to Treat Non-union Fracture. Curr Osteoporos Rep. 2018;16(2):155-168. doi:10.1007/S11914-018-0432-1/TABLES/2
4. Buza JA, Einhorn T. Bone healing in 2016. Clin Cases Miner Bone Metab. 2016;13(2):101-105. Accessed February 14, 2024. https://eds.p.ebscohost.com/eds/pdfviewer/pdfviewer?vid=0&sid=5f1ef49d-ee47-489c-a3b1-8d812580d7e8%40redis
5. Civitelli R, Armamento-Villareal R, Napoli N. Bone turnover markers: Understanding their value in clinical trials and clinical practice. Osteoporosis International. 2009;20(6):843-851. doi:10.1007/S00198-009-0838-9/FIGURES/1
6. Cox G, Einhorn TA, Tzioupis C, Giannoudis P V. Bone-turnover markers in fracture healing. doi:10.1302/0301-620X.92B3
7. Yoon BH, Yu W. Clinical Utility of Biochemical Marker of Bone Turnover: Fracture Risk Prediction and Bone Healing. J Bone Metab. 2018;25(2):73-78. doi:10.11005/JBM.2018.25.2.73
8. Cheng A, Vantucci CE, Krishnan L, et al. Early systemic immune biomarkers predict bone regeneration after trauma. Proc Natl Acad Sci U S A. 2021;118(8):e2017889118. doi:10.1073/PNAS.2017889118/SUPPL_FILE/PNAS.2017889118.SAPP.PDF
9. Chen JC, Jacobs CR. Mechanically induced osteogenic lineage commitment of stem cells. Stem Cell Res Ther. 2013;4(5):1-10. doi:10.1186/SCRT318/FIGURES/3
10. Duan Z wei, Lu H. Effect of Mechanical Strain on Cells Involved in Fracture Healing. Orthop Surg. 2021;13(2):369-375. doi:10.1111/OS.12885
11. Gibbs JC, McArthur C, Wark JD, et al. The Effects of Home Exercise in Older Women With Vertebral Fractures: A Pilot Randomized Controlled Trial. Phys Ther. 2020;100(4):662. doi:10.1093/PTJ/PZZ188
12. Flowers DW, McCallister E, Christopherson R, Ware E. The Safety and Effectiveness of Early, Progressive Weight Bearing and Implant Choice after Traumatic Lower Extremity Fracture: A Systematic Review. Bioengineering. 2022;9(12). doi:10.3390/BIOENGINEERING9120750/S1
13. Huang J, Zhang L, Lu A, Liang C. Organoids as Innovative Models for Bone and Joint Diseases. Cells. 2023;12(12):1590. doi:10.3390/CELLS12121590
14. Lancaster MA, Huch M. Disease modelling in human organoids. Dis Model Mech. 2019;12(7). doi:10.1242/DMM.039347
15. Vetsch JR, Betts DC, Müller R, Hofmann S. Flow velocity-driven differentiation of human mesenchymal stromal cells in silk fibroin scaffolds: A combined experimental and computational approach. PLoS One. 2017;12(7). doi:10.1371/JOURNAL.PONE.0180781

16. Leong PL, Morgan EF. Measurement of fracture callus material properties via nanoindentation. Acta Biomater. 2008;4(5):1569. doi:10.1016/J.ACTBIO.2008.02.030
17. Kingsmore KM, Vaccari A, Abler D, et al. MRI analysis to map interstitial flow in the brain tumor microenvironment □ Special Collection: Bioengineering of Cancer MRI analysis to map interstitial flow in the brain tumor microenvironment. APL Bioeng. 2018;2:31905. doi:10.1063/1.5023503
18. Clarke B. Normal Bone Anatomy and Physiology. Clinical journal of the American Society of Nephrology. 2008;3(3):131-139. doi:10.2215/CJN.04151206
19. Walsh JS. Normal bone physiology, remodelling and its hormonal regulation. Surgery. 2015;33:1-6. doi:10.1016/j.mpsur.2014.10.010
20. Aspden RM. Mechanical testing of bone ex vivo. Methods Mol Med. 2003;80:369-379. doi:10.1385/1-59259-366-6:369/FIGURES/4
21. Troy KL, Collins CJ. Bone Strength and Mechanical Behaviour. Comprehensive Structural Integrity. Published online January 1, 2023:3-17. doi:10.1016/B978-0-12-822944-6.00061-X
22. Safadi FF, Barbe MF, Abdelmagid SM, et al. Bone structure, development and bone biology. Bone Pathology. Published online 2009:1-50. doi:10.1007/978-1-59745-347-9_1/TABLES/2
23. Renders GAP, Mulder L, van Ruijven LJ, van Eijden TMGJ. Porosity of human mandibular condylar bone. J Anat. 2007;210(3):239-248. doi:10.1111/J.1469-7580.2007.00693.X
24. Keaveny TM, Morgan EF, Niebur GL, Yeh OC. Biomechanics of Trabecular Bone. Annu Rev Biomed Eng. 2001;3(1):307-333. doi:10.1146/ANNUREV.BIOENG.3.1.307
25. Cristofolini L, Angeli E, Juszczyk JM, Juszczyk MM. Shape and function of the diaphysis of the human tibia. J Biomech. 2013;46(11):1882-1892. doi:10.1016/J.JBIOMECH.2013.04.026
26. Mosekilde L, Mosekilde L, Danielsen CC. Biomechanical competence of vertebral trabecular bone in relation to ash density and age in normal individuals. Bone. 1987;8(2):79-85. doi:10.1016/8756-3282(87)90074-3
27. Linde F, Hvid I. The effect of constraint on the mechanical behaviour of trabecular bone specimens. J Biomech. 1989;22(5):485-490. doi:10.1016/0021-9290(89)90209-1
28. Boyle C, Kim IY. Three-dimensional micro-level computational study of Wolff's law via trabecular bone remodeling in the human proximal femur using design space topology optimization. J Biomech. 2011;44(5):935-942. doi:10.1016/J.JBIOMECH.2010.11.029
29. Fisher JS, Kazam JJ, Fufa D, Bartolotta RJ. Radiologic evaluation of fracture healing. Skeletal Radiol. 2019;48(3):349-361. doi:10.1007/S00256-018-3051-0/FIGURES/7
30. Leong PL, Morgan EF. Measurement of fracture callus material properties via nanoindentation. Acta Biomater. 2008;4(5):1569-1575. doi:10.1016/J.ACTBIO.2008.02.030
31. Maruyama M, Rhee C, Utsunomiya T, et al. Modulation of the Inflammatory Response and Bone Healing. Front Endocrinol (Lausanne). 2020;1:386. doi:10.3389/fendo.2020.00386
32. Schmidt-Bleek K, Schell H, Schulz N, et al. Inflammatory phase of bone healing initiates the regenerative healing cascade. Cell Tissue Res. 2012;347(3):567-573. doi:10.1007/S00441-011-1205-7/FIGURES/4
33. Fazzalari NL. Bone fracture and bone fracture repair. Bone Quality Seminars: Bone Fracture Healing and Strengthening. 2011;22:2003-2006. doi:10.1007/s00198-011-1611-4

34. Murao H, Yamamoto K, Matsuda S, Akiyama H. Periosteal cells are a major source of soft callus in bone fracture. J Bone Miner Metab. 2013;31(4):390-398. doi:10.1007/S00774-013-0429-X/FIGURES/6
35. Marsell R, Einhorn TA. THE BIOLOGY OF FRACTURE HEALING. Injury. 2011;42(6):551. doi:10.1016/J.INJURY.2011.03.031
36. Fischer V, Haffner-Luntzer M, Amling M, Ignatius A. CALCIUM AND VITAMIN D IN BONE FRACTURE HEALING AND POST-TRAUMATIC BONE TURNOVER. Eur Cell Mater. 2018;35:365-385. doi:10.22203/eCM.v035a25
37. Gao H, Huang J, Wei Q, He C. Advances in Animal Models for Studying Bone Fracture Healing. Bioengineering 2023, Vol 10, Page 201. 2023;10(2):201. doi:10.3390/BIOENGINEERING10020201
38. Cheng C, Shoback D. Mechanisms Underlying Normal Fracture Healing and Risk Factors for Delayed Healing. Curr Osteoporos Rep. 2019;17(1):36-47. doi:10.1007/S11914-019-00501-5/TABLES/1
39. Morshed S, Corrales L, Genant H, Miclau T. Outcome assessment in clinical trials of fracture-healing. Journal of Bone and Joint Surgery. 2008;90(SUPPL. 1):62-67. doi:10.2106/JBJS.G.01556
40. Nicholson JA, Yapp LZ, Keating JF, Simpson AHRW. Monitoring of fracture healing. Update on current and future imaging modalities to predict union. Injury. 2021;52:S29-S34. doi:10.1016/J.INJURY.2020.08.016
41. Conventional Xray – Aone Medical Equipment. Accessed April 9, 2024. https://aonemed.com/product/conventional-xray/
42. Mindray MX7 Ultrasound Machine | Best Price | UDS. Accessed April 9, 2024. https://www.ultrasoundportables.com/by-manufacturer/mindray/mindray-mx7
43. GE CT BrightSpeed 16 Parts, Repairs, Service. Accessed April 9, 2024. https://directmedparts.com/ge-ct-brightspeed-16-parts-repairs-service/
44. Firoozabadi R, Morshed S, Engelke K, et al. Qualitative and quantitative assessment of bone fragility and fracture healing using conventional radiography and advanced imaging technologies--focus on wrist fracture. J Orthop Trauma. 2008;22(8 Suppl). doi:10.1097/BOT.0B013E31815EA2A4
45. Bhandari M, Guyatt GH, Swiontkowski MF, Tornetta PI, Sprague S, Schemitsch EH. A Lack of Consensus in the Assessment of Fracture Healing Among Orthopaedic Surgeons. J Orthop Trauma. 2002;16(8):562-566. Accessed April 7, 2024. https://journals.lww.com/jorthotrauma/fulltext/2002/09000/Reamed_Versus_Nonreamed_Intramedullary_Nailing_of.00004.aspx
46. Dijkman BG, Sprague S, Schemitsch EH, Bhandari M. When is a fracture healed? Radiographic and clinical criteria revisited. J Orthop Trauma. 2010;24(SUPPL. 1). doi:10.1097/BOT.0B013E3181CA3F97
47. Panjabi MM, Lindsey RW, Walter SD, White AA. The Clinician's Ability to Evaluate the Strength of Healing Fractures from Plain Radiographs. J Orthop Trauma. 1989;3(1):29-32. Accessed April 7, 2024. https://journals.lww.com/jorthotrauma/abstract/1989/03010/the_clinician_s_ability_to_evaluate_the_strength.6.aspx

48. Bishop JA, Palanca AA, Bellino MJ, Lowenberg DW. Assessment of compromised fracture healing. Journal of the American Academy of Orthopaedic Surgeons. 2012;20(5):273-282. doi:10.5435/JAAOS-20-05-273
49. Bhattacharyya T, Bouchard KA, Phadke A, Meigs JB, Kassarjian A, Salamipour H. The accuracy of computed tomography for the diagnosis of tibial nonunion. Journal of Bone and Joint Surgery. 2006;88(4):692-697. doi:10.2106/JBJS.E.00232
50. Ricciardi L, Perissinotto A, Dabala M. Mechanical Monitoring of Fracture Healing Using Ultrasound Imaging. Clin Orthop Relat Res. 1993;293:71-76. Accessed April 7, 2024. https://journals.lww.com/clinorthop/abstract/1993/08000/mechanical_monitoring_of_fracture_healing_using.10.aspx
51. Moed BR, Subramanian S, van Holsbeeck M, et al. Ultrasound for the Early Diagnosis of Tibial Fracture Healing After Static Interlocked Nailing Without Reaming: Clinical Results. J Orthop Trauma. 1998;12(3):206-213. Accessed April 7, 2024. https://journals.lww.com/jorthotrauma/fulltext/1998/03000/Bone_Regeneration_with_Resorbable_Polymeric.13.aspx
52. Schwarzenberg P, Darwiche S, Yoon RS, Dailey HL. Imaging Modalities to Assess Fracture Healing. Curr Osteoporos Rep. 2020;18(3):169-179. doi:10.1007/S11914-020-00584-5/FIGURES/1
53. Den Boer FC, Bramer JAM, Patka P, et al. Quantification of fracture healing with three-dimensional computed tomography. Arch Orthop Trauma Surg. 1998;117(6-7):345-350. doi:10.1007/S004020050263/METRICS
54. D'Amelio P, Cristofaro MA, Grimaldi A, et al. The role of circulating bone cell precursors in fracture healing. Calcif Tissue Int. 2010;86(6):463-469. doi:10.1007/S00223-010-9362-3/FIGURES/5
55. Wancket LM. Animal Models for Evaluation of Bone Implants and Devices: Comparative Bone Structure and Common Model Uses. Vet Pathol. 2015;52(5):842-850. doi:10.1177/0300985815593124/ASSET/IMAGES/LARGE/10.1177_0300985815593124-FIG2.JPEG
56. Hixon KR, Mckenzie JA, Sykes DAW, et al. Ablation of Proliferating Osteoblast Lineage Cells After Fracture Leads to Atrophic Nonunion in a Mouse Model. Journal of Bone and Mineral Research. 2021;36(11):2243-2257. doi:10.1002/jbmr.4424
57. Garcia P, Histing T, Ignatius A. Rodent animal models of delayed bone healing and non-union formation: A comprehensive review. Eur Cell Mater. 2013;26(1):1-14. doi:10.22203/eCM.v026a01
58. Chaubey A, Grawe B, Meganck JA, et al. Structural and biomechanical responses of osseous healing: a novel murine nonunion model. Journal of Orthopaedics and Traumatology. 2013;14:247-257. doi:10.1007/s10195-013-0269-4
59. Kawaguchi H, Kurokawa T, Hanada K, et al. Stimulation of fracture repair by recombinant human basic fibroblast growth factor in normal and streptozotocin-diabetic rats. Endocrinology. 1994;135(2):774-781. doi:10.1210/EN.135.2.774
60. Kato T, Kawaguchi H, Hanada K, et al. Single local injection of recombinant fibroblast growth factor-2 stimulates healing of segmental bone defects in rabbits. Journal of Orthopaedic Research. 1998;16(6):654-659. doi:10.1002/JOR.1100160605
61. Yoon Y, Khan IU, Choi KU, et al. Different Bone Healing Effects of Undifferentiated and Osteogenic Differentiated Mesenchymal Stromal Cell Sheets in Canine Radial Fracture Model. Tissue Eng Regen Med. 2018;15(1):115-124. doi:10.1007/S13770-017-0092-8/FIGURES/6

62. Thomopoulos S, Zampiakis E, Das R, Silva MJ, Gelberman RH. The effect of muscle loading on flexor tendon-to-bone healing in a canine model. Journal of Orthopaedic Research. 2008;26(12):1611-1617. doi:10.1002/JOR.20689
63. Millis DL, Wilkens BE, Daniel GB, et al. Radiographic, Densitometric, and Biomechanical Effects of Recombinant Canine Somatotropin in an Unstable Ostectomy Gap Model of Bone Healing in Dogs. Veterinary Surgery. 1998;27(2):85-93. doi:10.1111/J.1532-950X.1998.TB00103.X
64. Volpon JB. Nonunion using a canine model. Archives of orthopaedic and trauma surgery . 1994;113:312-317.
65. Nakamura T, Hara Y, Tagawa M, et al. Recombinant Human Basic Fibroblast Growth Factor Accelerates Fracture Healing by Enhancing Callus Remodeling in Experimental Dog Tibial Fracture. Journal of Bone and Mineral Research. 1998;13(6):942-949. doi:10.1359/JBMR.1998.13.6.942
66. Kawaguchi H, Nakamura K, Tabata Y, et al. Acceleration of Fracture Healing in Nonhuman Primates by Fibroblast Growth Factor-2. The Journal of Clinical Endocrinology & Metabolism . 2001;86(2):875-880. Accessed April 9, 2024. https://academic.oup.com/jcem/article/86/2/875/2841144
67. Cook S, Wolfe M, Salkeld S, Rueger D. Effect of recombinant human osteogenic protein-1 on healing of segmental defects in non-human primates. The Journal of Bone & Joint Surgery . 1995;77(5):734-750. Accessed April 9, 2024. https://journals.lww.com/jbjsjournal/abstract/1995/05000/effect_of_recombinant_human_osteogenic_protein_1.10.aspx
68. Ehnert S, Rinderknecht H, Aspera-Werz RH, Häussling V, Nussler AK. Use of in vitro bone models to screen for altered bone metabolism, osteopathies, and fracture healing: challenges of complex models. Arch Toxicol. 2020;94(12):3937-3958. doi:10.1007/S00204-020-02906-Z
69. Themistocleous GS, Katopodis H, Sourla A, et al. Three-dimensional Type I Collagen Cell Culture Systems for the Study of Bone Pathophysiology. In Vivo (Brooklyn). 2004;18(6):687-696. Accessed April 9, 2024. https://iv.iiarjournals.org/content/18/6/687
70. Robey PG, Termine JD. Human bone cells in vitro. Calcif Tissue Int. 1985;37(5):453-460. doi:10.1007/BF02557826/METRICS
71. Takebe T, Wells JM. Organoids by design. Science (1979). 2019;364(6444):956-959. doi:10.1126/SCIENCE.AAW7567/ASSET/C4D79A2D-9343-43DB-A312-3665708442BE/ASSETS/GRAPHIC/364_956_F3.JPEG
72. Iordachescu A, Hughes EAB, Joseph S, Hill EJ, Grover LM, Metcalfe AD. Trabecular bone organoids: a micron-scale “humanised” prototype designed to study the effects of microgravity and degeneration. Microgravity. 2021;7(1). doi:10.1038/s41526-021-00146-8
73. Papadimitropoulos A, Martin I. A 3D in vitro bone organ model using human progenitor cells. Eur Cell Mater. 2011;21:445-458. doi:10.22203/eCM.v021a32
74. Park Y, Cheong E, Kwak JG, Carpenter R, Shim JH, Lee J. Trabecular bone organoid model for studying the regulation of localized bone remodeling. Sci Adv. 2021;7(4). doi:10.1126/SCIADV.ABD6495/SUPPL_FILE/ABD6495_SM.PDF
75. Hollister SJ. Porous scaffold design for tissue engineering. Nat Mater. 2005;4(7):518-524. doi:10.1038/nmat1421

76. Zhao F, Melke J, Ito K, van Rietbergen B, Hofmann S. A multiscale computational fluid dynamics approach to simulate the micro-fluidic environment within a tissue engineering scaffold with highly irregular pore geometry. Biomech Model Mechanobiol. 2019;18(6):1965-1977. doi:10.1007/S10237-019-01188-4/FIGURES/13
77. Lee J, Cuddihy MJ, Kotov NA. Three-Dimensional Cell Culture Matrices: State of the Art. Tissue Eng Part B Rev. 2008;14(1):61-86. doi:10.1089/teb.2007.0150
78. Pham QP, Sharma U, Mikos AG. Electrospinning of Polymeric Nanofibers for Tissue Engineering Applications: A Review. Tissue Eng. 2006;12(5):1197-1211. doi:10.1089/TEN.2006.12.1197
79. Moroni L, De Wijn JR, Van Blitterswijk CA. 3D fiber-deposited scaffolds for tissue engineering: Influence of pores geometry and architecture on dynamic mechanical properties. Biomaterials. 2006;27(7):974-985. doi:10.1016/J.BIOMATERIALS.2005.07.023

Chapter 3: Aim 1

3.1 Preamble

The following chapter is a collaborative paper in preparation for journal submission. Contributing authors are Elizabeth Hunt, Sera Choi, Zahra Bahranifard, Ed Shangin, Dr. Abby Whittington, Dr. Caitlyn Collins. I performed all DMA testing in this paper, and my specific contributions include the fracture healing and DMA testing background, DMA methodology, DMA results, and discussion and conclusion points related to mechanical analysis and pore size distribution.

Paper title: Dynamic micromechanical characterization of 3D printed bone in vitro models manufactured via vat photopolymerization

3.2 Introduction

Bone fractures are common and can occur because of injury, disease, or result from congenital disorders[1]. Typically, fractured bones are able to rebuild and repair if damage and fragment separation is sufficiently small, often classified in comparison to an experimentally determined critical size defect[2]. However, above this critical size, healing may be impaired, and use of a tissue scaffold has been shown to be beneficial in promoting healing by replacing the lost bone and minimizing the size of the defect[3]. Even with the use of bone grafts or tissue engineered scaffolds, bone healing is not guaranteed, resulting in delayed healing or even nonunion. Delayed fracture healing and nonunion are prevalent clinical complications with devastating impact on patient quality of life. These are challenging conditions to treat and lead to significant financial burden and reduced quality of life for the patient as the diagnosis of nonunion can be as late as one year post-fracture[4,5]. Bone tissue scaffolds are often created to be implanted into the body and mimic the body's internal environment to provide structural support for cells and promote migration, proliferation as well as nutrient and gas exchange. In such engineered constructs, the scaffold provides a significant portion of these cues; however, it is difficult to successfully

imitate each one of these cues in a single, replicable scaffold. Aside from the physiologic functions, there are also design aspects to consider such as pore size, geometry, and overall dimensions as these[6–8]. In addition to these shape characteristics, the mechanical properties such as storage modulus, loss modulus, and energy dissipation (tanδ) properties of the material and ultrastructure have been shown to impact cell viability and osteointegration[9]. All of these structural, material, and mechanical properties need to be accounted for when producing effective bone tissue engineered scaffolds. However, creating large (~ 1 cm) bone tissue scaffolds with fine geometric feature sizes (struct thickness ~200-400 µm; pore size ~250-450 µm) and uniformly distributed porosity using traditional stochastic techniques such as porogen leaching and gas foaming is not feasible as these methods generate randomly formed pores without any specific order or size gradation and ultrastructure[10]. This discrepancy has led to conflicting reports on the optimal pore size and geometry.

To overcome these drawbacks, it is necessary that reliable and precise printing methods and scaffold materials are explored for the advancement of bone tissue engineering and successful implantation. Vat photopolymerization (VP), an additive manufacturing method, possesses the capability to produce intricately designed geometries with exceptional precision and at relatively quick speeds[11]. These qualities render VP an appealing choice for constructing scaffolds used in tissue engineering applications. However, there is a scarcity of biocompatible printable materials that permit cell attachment and are of low enough viscosity for printing. Moreover, the few reported materials are not commercially available nor are they designed to replicate the bone microenvironment.

Current preclinical models for bone fracture healing rely on 2D cell culture and animal experiments, each with their own limitations regarding translation to patients[12]. Additionally, current detection strategies for delayed healing or nonunion such as radiolucency in planar x-rays and reported pain by the patient do not account for the *in* vivo mechanical environment[13,14], though studies have

shown a positive relationship between loading and bone healing[15,16]. 3D tissue culture systems such as organoids and 3D-cell culture models provide an *in vitro* tissue culture platform that allows for the prolonged study of human cells in an environment that mimics conditions in which tissue operates inside of the body[17]. In order to develop such a platform for assessing individual patient risk factors for non-union, three different 3D scaffold geometries were chosen—IsoTruss, Truncated Octahedron (TO), and Voronoi. Each geometry was chosen for its unique structural features: the IsoTruss for its high strength-to-weight ratio, enhanced mechanical stability, and similarity to traditional tissue scaffolds documented in previous literature; the Truncated Octahedron for its uniformity, porosity, and potential to promote uniform vascularization; and the Voronoi for its ability to mimic natural bone microenvironments. This study aims to characterize the mechanical properties manufactured using a novel, osteoconductive resin via vat photopolymerization (VP) and analyze their ability to facilitate cell proliferation throughout each scaffold.

3.3 Methods and Materials

Resin Formulation

A mixture of 50 wt% epoxidized soybean oil acrylate (ESOA, Sigma-Aldrich) and 50 wt% polyethylene glycol diacrylate (PEGDA, Sigma-Aldrich, MW = 575 g/mol) was used to formulate the resin for printing. Note, a 1 wt% diphenyl(2,4,6-trimethylbenzoyl)phosphine oxide photoinitiator (TPO, Sigma-Aldrich) and 0.20 wt% 2,5-bis(5-tert-butyl-benzoxazol-2-yl)thiophene UV absorber (BBOT, TCI Chemicals) were also added. These additions were to promote initiation of photopolymerization ensuring effective curing during 3D printing and to absorb any excess UV light that could penetrate deeper into the resin resulting in over-cure of the already cured layers, respectively.

Scaffold Printing

Model scaffolds of three different geometries (Voronoi, Truncated Octahedron, and Isotruss) were designed using nTopology (Figure 1.1). Scaffolds were created with an Autodesk Ember 3D printer, a VP bottom-up platform. The printer has a build area of approximately 40 x 64 mm with a maximum part height of 134 mm and a projected pixel size of 50 µm. The light source operated with a 5-watt power output and emitted light at a wavelength of 405 nm for an average of 2.5 seconds per layer. Every layer was 0.1 mm for a total dimension of 10 mm for the entire scaffold. The burn-in layers were removed and then the scaffolds were washed in 70% isopropyl alcohol (IPA) and additionally cured using a UV lamp (405 nm) for one minute.

Cell Seeding & Analysis

Prior to cell seeding, the scaffolds underwent sterilization using 70% ethanol for one hour without agitation, followed by three successive static washes (30 min each) with phosphate buffered saline (PBS, pH 7.4). A final wash was carried out using media made of αMEM and supplemented with 10% fetal bovine serum (FBS) and 1% penicillin-streptomycin-amphotericin (all from Thermo-Fisher).

An average of 1 x 10^5 NIH 3T3 fibroblasts (murine) were seeded on each tissue scaffold and left to attach for 30 minutes before adding 1 mL of media. A set (n = 4/geometry) was left to continue culturing for 4 and 7 days after seeding. The media was changed every two to three days. Subsequently, each sample was immersed for five minutes in 1 mL 10% formalin fixation solution. They were then rinsed with PBS for two minutes and then immersed in 1 mL of a post-fixation solution of 10% formalin for 20 minutes to fix the cells. Scaffolds were then rinsed again in PBS for one minute. Afterwards, they were stained with DAPI and Rhodamine Phalloidin dyes (both obtained from Thermo-Fisher) for an hour in the dark, and finally left in deionized water for a few hours.

The scaffolds were cut in half and examined using a laser scanning confocal fluorescence microscope (Zeiss Axio Observer.Z1) with 10x objective (Plan-Apochromat 10x/0.45 M27, Zeiss) and 60 µm diameter pinhole to assess spatial cell distribution and proliferation immediately after seeding and following 4 and 7 days of culture. The confocal images were tiled using a 5 x 5 (4000 µm x 4000 µm) and z-stacks were captured for a total of images 38 slices with a depth of 201.6 µm (5.45 µm slice thickness). An automatic filter (Zen Black) was applied to eliminate background fluorescence caused by the scaffolds' autofluorescence at 461 nm. Subsequently, ImageJ was employed to further eliminate any residual background fluorescence improving the precision of the cell nuclei counting process. After seeding the scaffolds and incubating them in the culture media for multiple days, noticeable swelling was observed in the IsoTruss scaffolds, while limited swelling was observed in the other two geometries. The scaffolds emitted blue autofluorescence during imaging with the confocal microscope, which interfered with the DAPI channel and being able to count nuclei (Figure 3.3). The rhodamine channel was used to validate the presence and proliferation of cells by tracking actin.

Dynamic Mechanical Analysis

Dynamic mechanical analysis (DMA, ElectroForce 3200) was performed on seeded (n = 6/geometry for 4- and 7-day of culture) and unseeded (n = 1/geometry) scaffolds via cyclic compression using a strain sweep to analyze how microstructure impacts the organoid storage modulus (E'), loss modulus (E"), and damping coefficient (tan δ). The strain sweep was conducted at a frequency of 0.1 Hz starting with a dynamic amplitude of 0.2 mm (4% strain) and increasing by 0.1 mm until reaching 1 mm dynamic amplitude (10% strain). All testing was performed submerged in a 1x concentrated phosphate-buffered saline (PBS, pH 7.4) solution at 37 °C (Figure 3.1).

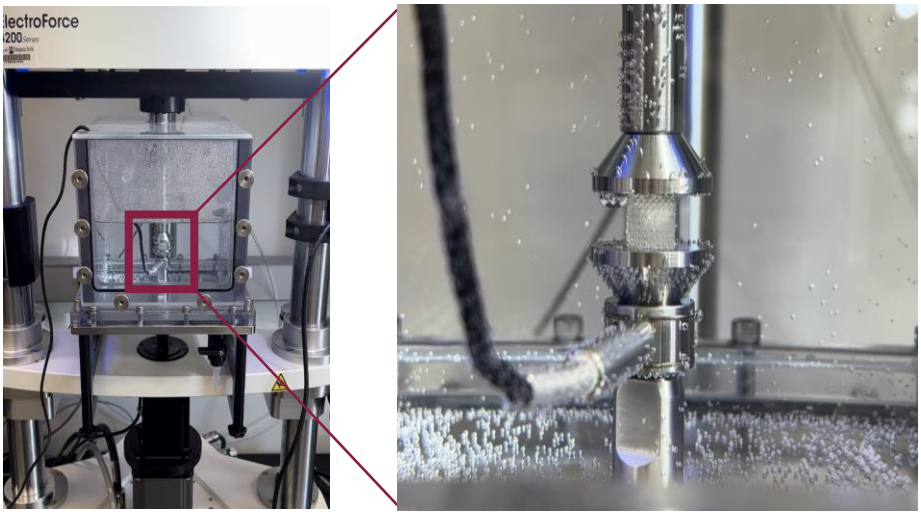

Figure 3. 1: DMA compression testing setup (ElectroForce 3200) outfitted with a temperature controlled water bath filled with 1x concentrated phosphate-buffered saline (PBS, pH 7.4) solution at 37°C.

Statistical Analysis

Mechanical data was analyzed using a three-way ANOVA test (Python) to determine significant differences between geometry, time soaked, and whether or not the scaffolds were seeded with cells. An additional two-way ANOVA post hoc analysis was also performed to determine significant differences between individual groups ($\alpha = 0.05$). Cell count data were compared using a two-way ANOVA test through R Studio.

3.4 Results

Printing

After printing, each scaffold type closely resembled its modeled geometry (e.g. Figure 1.1) and their 10 mm cubic dimensions, as seen in Figure 3.2. For the three geometries the average printing time was two and a half hours. However, during the printing process, challenges were encountered with the IsoTruss geometry. Approximately half of the total printed IsoTruss scaffolds, after undergoing the printing, washing, and curing steps were rendered malleable and fragile. As a result, the IsoTruss geometry had two fewer replicates (n = 4) compared to the Truncated Octahedron and Voronoi

geometries (n = 6). Average pore diameters were 579, 397, and 662 µm for the Voronoi, IsoTruss, and TO scaffolds, respectively, within range of the targeted print size.

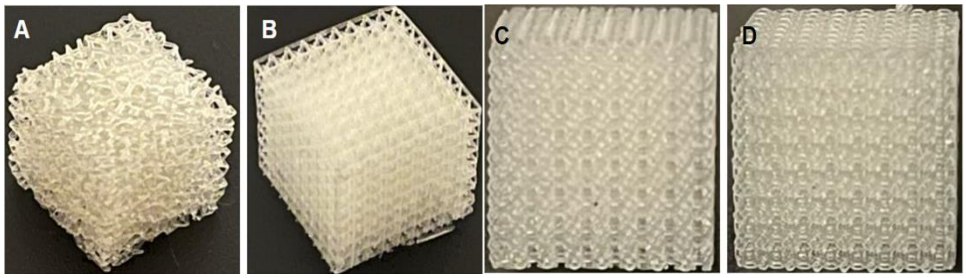

Figure 3. 2: Representative scaffolds printed with 50% wt. ESOA and 50% wt. PEGDA in three different geometries: Voronoi (A); IsoTruss (B); and Truncated Octahedron (C & D) lattice structures.

Cell Seeding, Proliferation, and Counting

In the IsoTruss scaffolds, significant spatial-dependent proliferation was evident, with peripheral regions exhibiting more substantial cell growth by the seventh day (Figure 3.4A). The cell counts at the outermost regions (-1200 to -400 and 1200 to 2000 µm) were markedly higher on day 7 compared to day 4. However, the overall progression from the 4 day to the 7 day culture period did not demonstrate the expected increase in cell counts. This stagnation in growth suggests a potential plateau in cellular activity. Truncated Octahedron scaffolds showed a remarkable increase in cell proliferation at the 7 day mark across all distances, with the central region (-400 to 400 µm) displaying a significant rise in cell count compared to the 4 day culture (Figure 3.4B). Voronoi scaffolds exhibited the most pronounced effect of culture duration on cell proliferation, with all regions, particularly the periphery, showing a higher cell count at day 7 (Figure 3.4C).

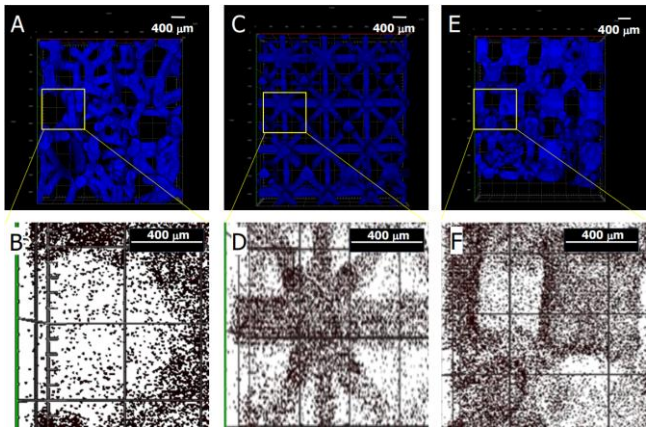

Figure 3. 3: Voronoi (A & B), IsoTruss (C & D), and TO (E & F) scaffolds DAPI (top) and Rhodamine (bottom) stained after seeding for seven days with 3T3 cells.

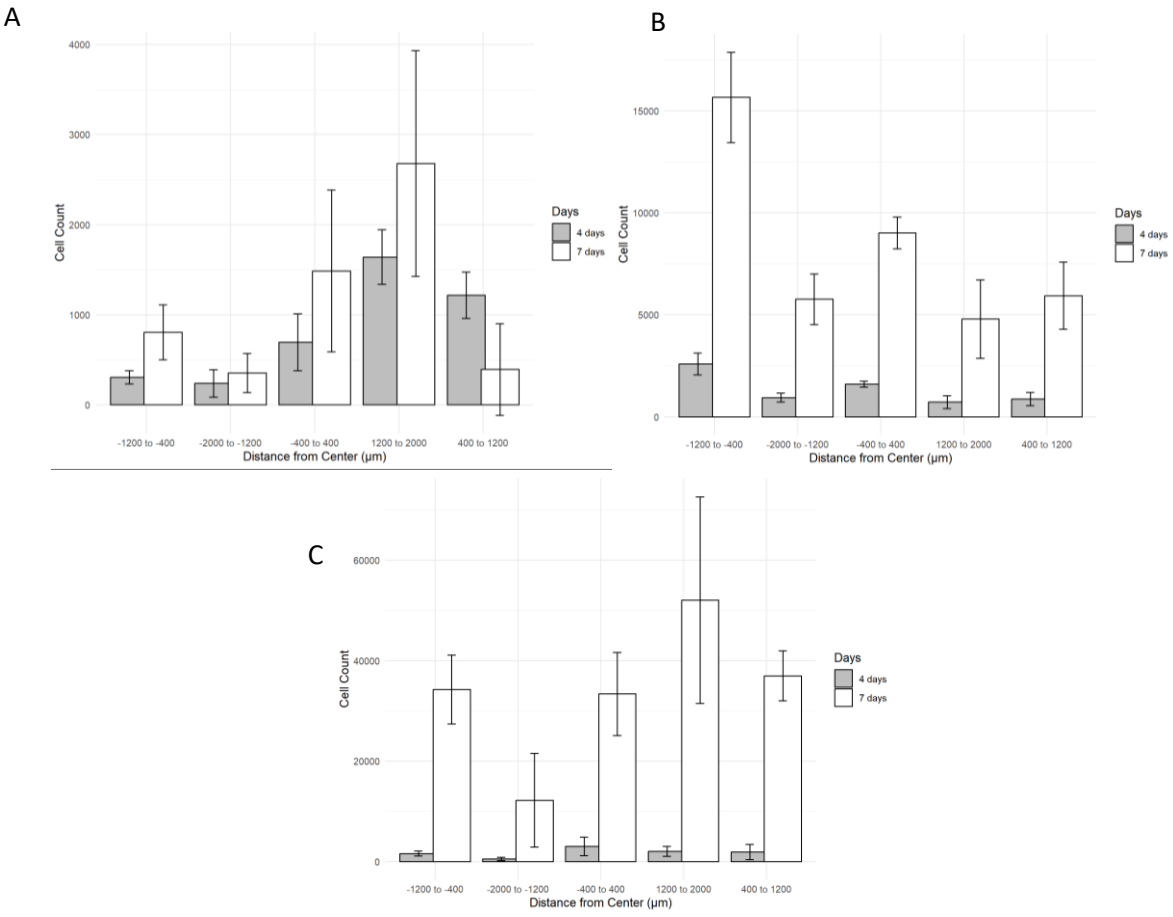

Figure 3. 4: Cell count distribution within IsoTruss (A), TO (B), and Voronoi (C) scaffolds over 4 and 7 days.

The two-way ANOVA conducted on the Isotruss scaffold indicated no significant effect of 'Distance' on the dependent variable ($F(4, 30) = 1.076$, $p = 0.386$), suggesting that different locations within the scaffold did not significantly affect cell behavior. However, 'Days' showed a highly significant effect ($F(1, 30) = 70.240$, $p < 2.36e-09$), indicating that the time after cell seeding significantly impacted the measured outcome. The interaction between 'Distance' and 'Days' was not significant ($F(4, 30) = 0.815$, $p = 0.526$), suggesting that the effect of time on the dependent variable did not vary significantly across different scaffold locations.

In the case of the Truncated Octahedron scaffolds, the two-way ANOVA indicated highly significant effects of both distance ($F(4, 50) = 58.25$, $p < 2e-16$) and days ($F(1, 50) = 508.17$, $p < 2e-16$), along with a significant interaction between these factors ($F(4, 50) = 28.86$, $p = 1.88e-12$). These findings suggest a strong spatial and temporal influence on cell outcomes, with the interaction highlighting the complexity of cell responses to scaffold characteristics over time.

For the Voronoi scaffolds, significant effects were observed for distance ($F(4, 50) = 10.003$, $p = 5.01e-06$) and days ($F(1, 50) = 232.806$, $p < 2e-16$), as well as for their interaction ($F(4, 50) = 8.558$, $p = 2.43e-05$). These results demonstrate a significant spatial and temporal impact on cell behavior, with an important interaction effect suggesting that the influence of one factor is contingent on the level of the other.

Dynamic Mechanical Analysis

Some of the IsoTruss scaffolds (n = 2) failed prematurely during the DMA testing due to inconsistencies in the printing, these were excluded from further analyses. For the remaining scaffolds, average storage modulus increased from day 4 to 7 of static culture (Table 3.1), and generally decreased for each scaffold as oscillation strain increased (Figure 3.5). The stiffest storage modulus achieved overall was reached by a 7-day cultured IsoTruss scaffold (2.70 MPa). Note, variation in the storage modulus for

the 7-day IsoTruss scaffolds was the highest (1.27 MPa). A three-way ANOVA test conducted on the storage moduli of seeded and controlled non-seeded scaffolds (n = 3 for each geometry and days seeded), revealed a significant difference in stiffness between seeded and non-seeded scaffolds (p = 0.000453). Two-way ANOVA post hoc analysis further revealed that the Voronoi scaffolds had the only significant and consistent increase in storage modulus between 4- and 7-day cultures (p = 0.0293), which is illustrated in Figure 3.6.

Table 3. 1: Storage modulus (MPa) of the three scaffold geometries for 4- and 7-day cultures and soaked controls (mean±SD)

Day	Seeded with cells?	n	IsoTruss	TO	Voronoi
0	No	1	1.08	0.46	0.91
	No	3	2.18 ± 0.91	1.49 ± 0.31	1.09 ± 0.14
4	Yes	6	0.80 ± 0.53*	0.64 ± 0.40	0.55 ± 0.25
	No	3	1.24 ± 0.39	1.85 ± 0.47	0.88 ± 0.21
7	Yes	6	0.81 ± 1.27*	0.69 ± 0.35	1.19 ± 0.57
	*n = 4 for IsoTruss 4- and 7-day culture mechanical testing				

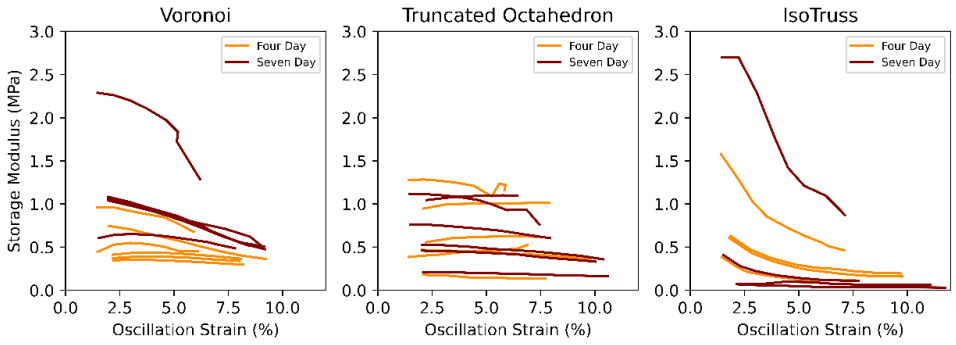

Figure 3. 5: Storage modulus (MPa) vs. oscillation strain (%) for Voronoi, TO, and IsoTruss scaffolds.

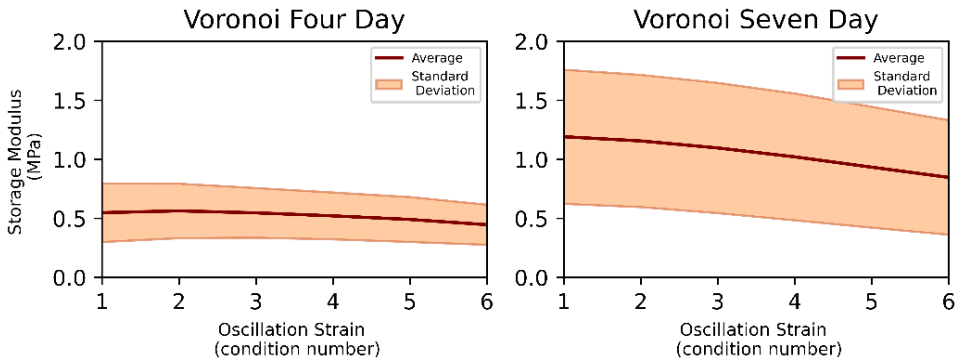

Figure 3. 6: Average and standard deviation storage modulus (MPa) vs. oscillation strain (condition number) for Voronoi four (left) and seven (right) day seeded scaffolds. The condition number for oscillation strain refers to the dynamic amplitude being assessed, starting at 2 mm and increasing by 1 mm for each condition.

The peak storage modulus for the Voronoi 7-day cultured scaffolds is 2.26 MPa. The peak storage modulus is achieved by a 4-day cultured scaffold for the TO geometry at 1.28 MPa at 2.14% oscillation strain. Trends in loss modulus were consistent among the Voronoi and TO scaffolds, with a general increase with increased oscillation strain. On average, the loss modulus of IsoTruss scaffolds decreased at higher oscillation strains, leading to an average tanδ of 0.0613 at 2% strain, which is over 2 times greater than Voronoi (0.0227) and TO (0.0297) at the same strain. Figure 3.7 highlights this distinction between the IsoTruss scaffolds compared to the Voronoi and TO.

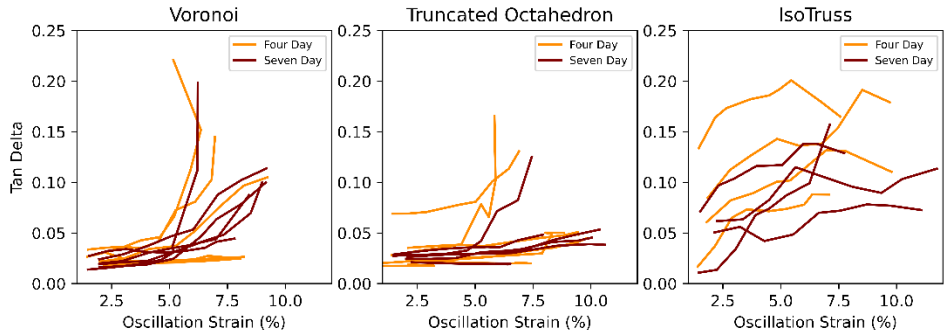

Figure 3. 7: Tan delta vs. oscillation strain (%) for Voronoi, TO, and IsoTruss scaffolds.

3.5 Discussion

This study aimed to explore the influence of scaffold geometry on cell distribution and proliferation in the context of bone tissue engineering, with an emphasis on the structural and mechanical properties of the scaffolds post-seeding. Our results indicate that scaffold geometry has a profound impact on cell behavior, as well as on the mechanical properties of the scaffolds, which varied with storage moduli within the range of soft fracture callus tissue. Scaffold stiffness varied, with storage moduli on the order of soft fracture callus tissue after seeding (fracture callus moduli: 0.5-1000 MPa[18]).

Despite the limited number of samples available for mechanical testing, trends emerged that provided insight into the effects of cell seeding on scaffold stiffness. The IsoTruss scaffolds demonstrated a maximum storage modulus among 7-day seeded scaffolds, yet exhibited significant variability with the rest of the 7-day samples being softer than the average Truncated Octahedron (TO) and Voronoi scaffolds. The variability and instances of softness in IsoTruss scaffolds may be attributable to inconsistencies in printing parameters or the curing process, with some scaffolds being too soft for DMA testing. These findings align with the cell distribution data, where IsoTruss scaffolds showed non-uniform cell distribution and a marked increase in cell proliferation from the center towards the periphery which was significantly more pronounced by day 7, which could be attributed to the cells' mechanotransducive responses to the more malleable sections. The high standard deviation rate is most likely due to those varied malleability rates for each scaffold (Figure 3.4A). The contrast in damping factor between IsoTruss scaffolds and TO and Voronoi scaffolds indicates that the different geometries have an impact on the micromechanical environment of the scaffolds. Energy is being absorbed and dissipated by the IsoTruss scaffolds much faster, which could indicate a buckling movement by the struts of the scaffolds that is not mimicked in the other two geometries.

The Truncated Octahedron scaffolds showed a dynamic pattern of cell distribution over time, with a distinct peak in cell count at mid-range distances from the center on day 4, with the peak becoming less distinct by day 7 as cell counts leveled across distances. The reduced variability on day 7 points towards an evening out of cell distribution, which may be due to cells filling the spaces more uniformly as they proliferate (Figure 3.4B). The initial peak suggests that certain features of the scaffold's geometry at these distances may be particularly conducive to initial cell attachment or proliferation.

The Voronoi geometry supported significant cell proliferation, with the highest cell counts observed at the outermost distance range on both day 4 and day 7, which may be related to the scaffold's mechanical stability and consistent microenvironment (Figure 3.4C). This indicates that the Voronoi geometry could provide an environment that supports or encourages cell growth, particularly in the peripheral regions.

A possible limitation to the DMA procedure is that it assumes uniform shape of the scaffolds in order to calculate storage modulus, loss modulus, and tanδ. Because storage modulus is the force divided by cross-sectional area (CSA), the dimensions of the scaffolds is important here. Although all scaffolds are printed with consistent dimensions that are used in these calculations, factors such as swelling and printing infidelity can alter the CSA of the scaffolds. This limitation arose when a stiffer IsoTruss sample was visually larger than the other samples. The data can be normalized, however, through a simple scaling multiplication of the ideal cross sectional area (0.0001 m^2) divided by the measured CSA. This normalization was conducted for one control IsoTruss scaffold that was substantially larger than the others. In the future, all samples should be measured and normalized to their own CSA.

Collectively, these results underscore the importance of an integrated approach in scaffold design, where both the geometric and mechanical aspects are optimized to support cell behavior conducive to tissue regeneration. It suggests that scaffold geometry is a critical factor in determining cell

distribution and proliferation, which has significant implications for the design of future scaffolds for bone tissue engineering. A scaffold's ability to support uniform cell growth and distribution is crucial for the successful integration and functioning of the engineered tissue. The observed spatial effects on cell behavior within the Truncated Octahedron and Voronoi scaffolds, and the significant temporal effects across all scaffold types, emphasize the importance of considering both the initial scaffold design and the dynamic nature of cell growth over time. Further spatial analysis of the cell distribution may also provide insight into the differences observed between scaffold geometries and culture time. The results of this study represent a successful first step at generating an organoid that recapitulates the micromechanical environment of healing bone. The investigated scaffold geometries 3DP via VP using the novel ESOA and PEGDA resin resulted in successful cell adhesion, proliferation, and extracellular matrix deposition, providing valuable insight into the structure/function relationship of pore shape and bone organoid mechanical properties.

3.6 Conclusion

The current study analyses the cell proliferation and mechanical properties of three different scaffold geometries after being seeded for four and seven days with 3T3 fibroblast cells. This analysis will eventually lead to a bone organoid platform in which individual patient risk factors for non-union can be studied. After successful cell adherence, dynamic mechanical analysis confirms that the storage moduli of the scaffolds are within range of soft fracture callus tissue. More data will be collected with additional scaffolds, as well as unseeded scaffolds soaked for four and seven days as control groups. Future studies related to this research will involve computational fluid dynamics to investigate extracellular matrix-forming wall shear stress produced by fluid flow.

3.7 Acknowledgements

We acknowledge support from the Beckman Scholar Foundation and the National Center for Advancing Translational Science of the NIH Award UL1TR003015/KL2TR003016.

Chapter 4: Aim 2

In order to begin optimization of fluid flow, we turn to computational modeling to determine the distribution of wall shear stress (WSS) acting across the 3D scaffold surfaces. Average WSS values of 0.55 mPa to 24 mPa have been shown to drive mineralization in *in vitro* bone cell culture[19]. As such, my second aim seeks to develop a validated computational model to simulate fluid flow within an organoid, such that the predicted WSS values can be used to determine optimal perfusion flow conditions. This aim can be broken down into two parts: (1) the generation of validation data using dynamic contrast enhanced magnetic resonance imaging (DCE-MRI) to quantify flow velocity and direction throughout the 3D scaffolds, and (2) the modeling and computational fluid dynamics (CFD) simulation of laminar flow through the 3D scaffolds.

4.1 Methods and Materials

4.1.1 DCE-MRI Validation Data

To perform DCE-MRI analysis, the porous scaffolds needed to be filled with a hydrogel that would prolong the flow of contrast through the scaffold for the entire duration of the scan (~ 12 minutes). The highly porous scaffolds are a challenging material to fill completely, without any air pockets in the large pores; so, three different methods were tested for filling the scaffolds. These include a pour over method, desiccator method, and pressure differential method.

Hydrogel Preparation

To secure the 3DP scaffolds within the tissue culture inserts and reduce the rate of fluid flow through the porous scaffolds, a methodology for photoHA/collagen hydrogel preparation, developed in the Munson Lab by Jen Hammel, was adapted and performed. This hydrogel was used for the scaffolds filled via the pour over method. First, the collagen solution was prepared by combining 1318 µl of collagen I, 30 µl of 1N NaOH, 1278 µl of sterile water, and 292 µl of 10x concentrated phosphate buffered solution (PBS). Next, 1460 µl of basal vasculife media, 2920 µl of 1% PhotoHA, and 58.4 µl of LAP (lithium

phenyl-2,4,6-trimethylbenzoylphosphinate) were added to the collagen solution and mixed using a 100 µL volume pipet.

For the pressure differential and desiccator methods, a gelatin hydrogel which did not require UV curing was used. The hydrogel was prepared by mixing 0.5 g of gelatin from porcine skin (Sigma-Aldrich®, gel strength ~ 300 g bloom, Type A) with 9 mL of DI water. A few ratios of gelatin to water were tested (data not included) before deciding on this balance as it formed a hydrogel that was easy to pour and solidified in a suitable timeframe. The gelatin powder was poured into slightly warmed DI water (37°C) while mixing at a slow speed on a stir plate. The solution had to be stirred slowly to reduce the introduction of air bubbles into the hydrogel. After stirring and warming for 30 minutes, all of the gelatin was dissolved and the hydrogel was ready to be used. Once removed from the stir and heat plate, the hydrogel had to be poured immediately in order to avoid premature solidification.

Transwell/Scaffold Filling – Pour Over Method

The imaging for MRI fluid flow analysis is done in a Millicell® Standing Cell Culture Insert (diameter = 12 mm, pore size = 8.0 µm). For the scaffolds to fit inside and fill the inserts, they must have a 10 mm diameter and 3 mm height. Our 3DP geometries have not yet been generated for cylindrical scaffolds. As such, 10 mm x 10 mm x 10 mm cubes were manually trimmed with a scalpel to fit the cell culture insert. After trimming, the scaffolds were rinsed with deionized (DI) water to eliminate any debris.

Approximately 100 µL of photoHA/collagen hydrogel solution was added to the transwells already containing the scaffolds, to fill the open pores and reduce the chances of fluid diverting around the scaffold rather than passing through it. The filled inserts were cured with a 385 nm lamp and placed in an incubator for 30 minutes. Trial and error was utilized on some test samples (n=2) to modify the

hydrogel filling procedure prior to curing to improve penetration of the hydrogel throughout the scaffolds using the pour over method. In order to settle the hydrogel better in the scaffold pores, the transwell was agitated by manually shaking the well plate and evacuation of air bubbles was attempted by using a syringe to pull trapped air from within the scaffold up to the surface where it could be scraped off.

Transwell/Scaffold Filling – Desiccator Method

For this method, the scaffolds were cut into 3 mm tall slices, and remained in their square shape. After slicing, the scaffolds were placed into a 24 well plate and soaked in 10x PBS solution for at least 2 hours to try to reduce surface tension and adhesion of air bubbles during filling (Figure 4.1). Once the hydrogel was ready to pour, the scaffolds were transferred to wells without PBS solution with forceps. The hydrogel was taken directly from the stir and heat plate to be poured over the scaffolds, filling each well so that the scaffold was completely submerged. After pouring, the well plate was agitated by manually shaking it in order to bring any large air pockets to the surface and settle the hydrogel to the bottom of the scaffolds. Immediately after shaking, the well plates were placed in the desiccator for 1 hour at a pressure of 9.8 PSI.

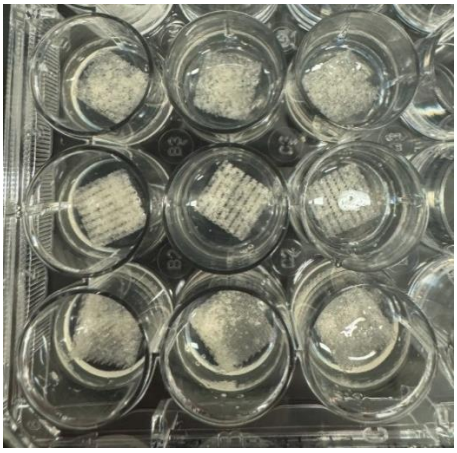

Figure 4.1: Scaffold slices soaking in 10x PBS solution.

Transwell/Scaffold Filling – Pressure Differential Method

Finally, a syringe pump and tubing were used to generate a pressure differential across the scaffolds to pull the air bubbles out of the hydrogel/scaffold mixture. This procedure was performed in transwell inserts (Costar®, diameter = 6.5 mm, pore size = 3.0 μm), so the scaffolds needed to be trimmed into a cylindrical shape. Rather than measuring and trimming manually, the polyester membrane was removed from one transwell insert and it was used as a punch to get an accurate size scaffold (Figure 4.2). After punching through the center of a 10 mm x 10 mm x 10 mm cube, the cylinder was cut into 3 mm high individual cylinders.

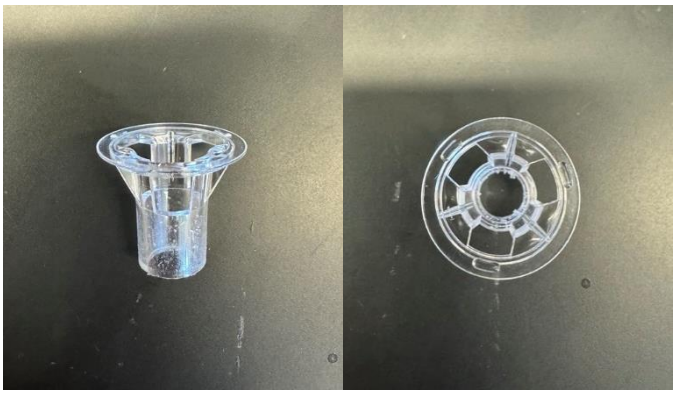

Figure 4.2: 6.5 mm diameter scaffold punch made from transwell insert.

The cylindrical scaffolds were then rinsed with 10x PBS to clear any debris and soaked in 10x PBS for at least 2 hours in a transwell plate. After soaking, the scaffolds were placed into the 6.5 mm transwell inserts so that they fit snuggly in the bottom. Flexible tubing with a 6 mm diameter was then fit around the transwell insert containing the scaffold, and the other end of the tubing was fit onto a 60 mL syringe (Figure 4.3). Once both ends of the tubing were sealed, the prepared hydrogel was taken directly off the stir and hot plate and poured over the scaffold using a smaller 5 mL syringe for more control. After the hydrogel settled, air was carefully extracted through the polyester membrane by slowly pulling out the syringe plunger (Figure 4.3). If there were still visible air bubbles remaining in the scaffold, more

hydrogel was poured over the scaffold and pulled through using the syringe plunger. Once the scaffold was completely filled, the tubing was first removed from the syringe and then the transwell insert. Filled scaffolds were then left to cure in transwell plates.

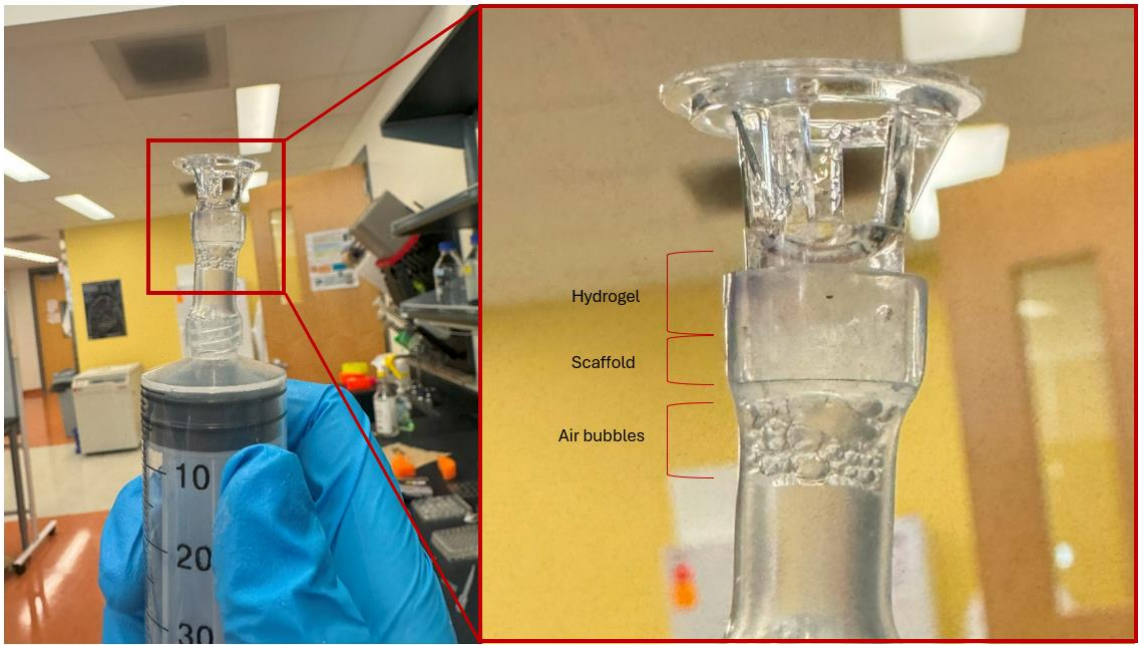

Figure 4.3: Pressure differential method setup. The air bubbles in the tubing show the air pockets being pulled through the membrane and into the tubing.

Scaffold Evaluation

Scaffolds were evaluated for air pockets with three methods: visual evaluation, MRI grayscale intensity, and microscopy. Visual evaluation was the first indicator of air pockets trapped within the scaffold after filling. They appeared as lighter regions, usually within the center of the scaffold. Air pockets were also visible via MRI in which the grayscale intensity depicted regions with air pockets. Lastly, brightfield and DAPI microscopy scans were also taken to assess the presence of air in the scaffolds.

DCE-MRI

DCE-MRI, an imaging technique used to measure interstitial fluid flow by tracking the movement of contrast agents (gadolinium) through hydrogel[20] was utilized to measure fluid velocity and direction through our hydrogel-filled scaffolds filled via the pour over method (n=2 for Voronoi, n=1 for IsoTruss). DCE-MRI was only performed on these scaffolds due to MRI maintenance and repairs. This methodology is described in detail by Kingsmore et al. Briefly, 200µL of 1:100 gadolinium contrast agent was applied to the surface of the hydrogel-filled scaffolds using an infusion rate of 500 µL/min; T2 sequence MRI imaging was then performed using a field of view of 19.2 mm x 22 mm, image size of 192 x 220 pixels, spatial resolution of 0.1 mm/pixel, temporal resolution of 2 min 54 s and 300 ms with 5 s for adjustments, and slice thickness of 3 mm. A single baseline scan was taken before adding the gadolinium contrast, and then four subsequent post-scans were taken 30 s after gadolinium injection. The resultant images were then processed using a custom Matlab code developed by Kingsmore et al. The DCE-MRI analysis assumes that the flow velocity of gadolinium through the scaffold and hydrogel is equal to the fluid velocity flow within the hydrogel. Through the proportional relationship that MRI signal intensity has with gadolinium concentration, the velocity field (magnitude and direction of fluid flow) is calculated using their computational model by tracking changes in pixel intensity from baseline through each follow-up image. Thus, tracking the flow of contrast through the scaffold over time and enabling the back calculation of fluid flow velocity and direction throughout our complex porous scaffolds.

Echo Microscope

In order to evaluate the pressure differential method for effectively filling the scaffolds, imaging of the scaffolds was performed on the Echo Revolution microscope (n=1 for each geometry). The scaffolds were stained with DAPI from a prior experiment (Chapter 3, Section 3.3), so imaging was done in both the fluorescent DAPI and Trans (brightfield) channels using 10x magnification. All regions of the

scaffolds were inspected for air pockets, and sample captures were taken at various locations throughout the three samples.

4.1.2 CFD Model

For the CFD model methodology and results, I will focus on the IsoTruss geometry because we were only able to generate validation DCE-MRI data for the IsoTruss geometry due to machinery maintenance and repair.

Saffold Geometry

Three different options were explored as starting points to form the 3D solid models of the IsoTruss scaffolds: the original stereolithography (STL) files that the scaffolds are printed from, STL files formed on Fiji from confocal microscope scans, and 3D CAD models generated in SolidWorks. The format that was ultimately imported into COMSOL to run the simulations was a 3D manufacturing format (3MF) modeled from a solid body formed in SolidWorks from the original, ideal STL IsoTruss file.

In order to model this geometry, the ideal STL IsoTruss file was first imported into SolidWorks, and converted into a SolidWorks part file (PRT) by drawing and extruding a 10 mm x 10 mm x 10 mm cube over top the structure. The STIL file was subtracted from the solid cube to generate a PRT file for the pore space of the scaffold. To return to the structure, another cube was formed and the subtraction function was repeated (resulting body shown in Figure 4.4A). This 3D body was trimmed to the smallest repeating unit, and measurements were taken on SolidWorks of the dimensions to create a custom model of the unit cell (Figure 4.4B). This smoothed out the surfaces, eliminating the intricate triangles (seen on the struts of Figure 4.4A). Because the model simulates movement of fluid around the struts, the 3D body imported into COMSOL was the resulting pore space (Figure 4.4C-E). 3MF files were the most compatible with COMSOL, so the final pore space model was trimmed into slices and saved as 3MF files to be imported into COMSOL.

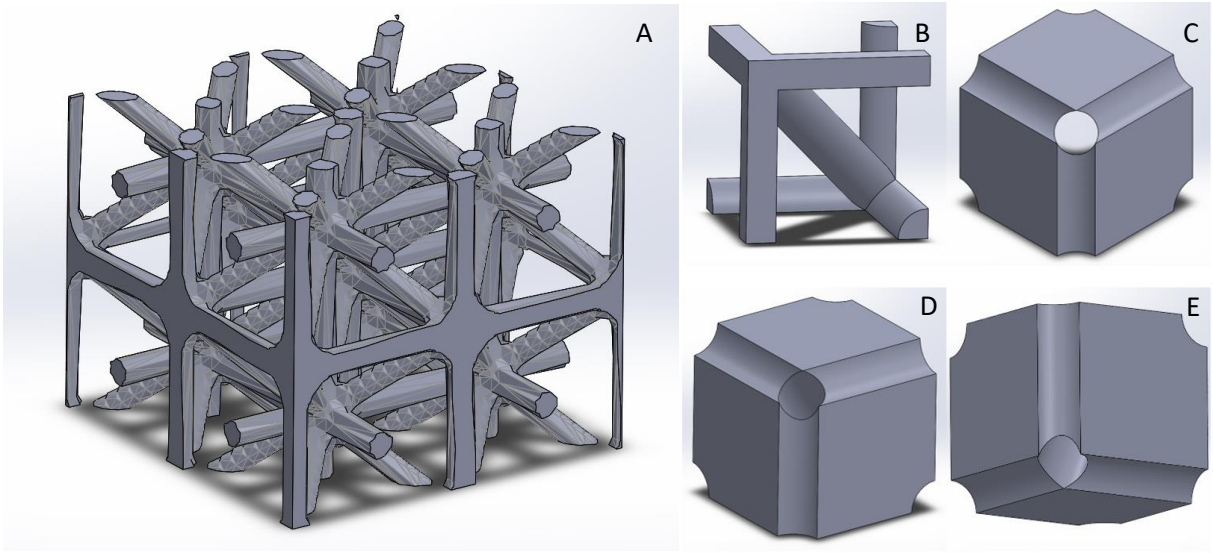

Figure 4.4: Portion of IsoTruss ideal CAD rendering (A), modeled basic unit of IsoTruss struts (B), and three views of pore space around basic unit struts (C-D).

Setup in COMSOL

Once an importable version of the geometry was created, the simulation was set up in the COMSOL software. The first step was to choose the type of study being conducted—in this case it was a stationary laminar fluid flow simulation. Because we wanted to mimic the flow of solution through a scaffold in a bioreactor setting, the flow rate will not change throughout the culture, so stationary flow maintains a constant inlet velocity throughout the simulation. The selection of laminar flow, as opposed to turbulent flow, was based on a few different factors. The type of flow is calculated by determining the Reynolds Number (Re), where ρ is fluid density, v is velocity, L is characteristic length, and μ is dynamic viscosity (Eq. 1).

$$Re = \frac{inertial\ forces}{viscous\ forces} = \frac{\rho v L}{\mu} \qquad (1)$$

For laminar flow, Re is less than 2000, and for turbulent flow it is greater than 4000. The Re calculated for this simulation was very small, indicating laminar flow through the pores of the scaffolds. Additionally,

we want to achieve laminar flow through the scaffolds in the bioreactor system, which made this the best choice for the simulation.

Once the type of simulation was chosen, the COMSOL GUI guided the setup and simulation, starting with the geometry. After importing the particular slice being simulated, COMSOL converted the 3MF file to a solid body and then there were a few modifications that needed to be made to ensure the dimension and direction were correct. For these simulations, the built-in COMSOL library material that was most similar to the material that will be used in the bioreactor (PBS) was water, so that was selected as the material in the pore space.

With the 3D body set up, the physics of the laminar flow simulation could be developed. An assumption that was made in the laminar flow model is that there was incompressible flow in the liquid. This is a valid and accepted assumption for most liquids, and assumes that the density of the fluid is constant throughout the simulation, which was true for this study. Equations 2-4 are the Navier-Stokes governing equations used for this simulation, where **ρ** is equal to fluid density, ***u*** is equal to the fluid velocity, and **p** is equal to fluid pressure.

$$\rho(\boldsymbol{u}\cdot\nabla)\boldsymbol{u} = \nabla\cdot[-p\boldsymbol{I}+\boldsymbol{K}]+\boldsymbol{F} \quad (2)$$

$$\rho\nabla\cdot\boldsymbol{u} = 0 \quad (3)$$

$$\boldsymbol{K} = \mu(\nabla\boldsymbol{u}+(\nabla\boldsymbol{u})^{\boldsymbol{T}}) \quad (4)$$

The next selection made was the boundary source of inlet and outlet velocity. Two simulations were conducted, one with flow coming from the top boundary only and one with flow coming from the top and side boundary. The outlet boundary that was selected for both simulations was the bottom surface.

In selecting average velocities to simulate in this model, it assumed that the velocity was fully developed at the inlet and moved from the selected top boundary of the unit to the bottom. Five inlet velocities were simulated: 0.05, 0.10, 0.15, 0.20, and 0.25 mm/s. For each inlet velocity, the simulation had to be re-computed. A coarse mesh was created for this 3D body.

COMSOL Simulation and WSS Calculation

After the simulation was completed, the results were manipulated to display various calculations or derive additional metrics to display. The metrics chosen to display after the simulation was completed were velocity, direction, and WSS. WSS (τ) was calculated with the following equation:

$$\tau = \gamma\mu \qquad (5)$$

where γ is the shear rate and μ is the dynamic viscosity. On COMSOL this calculation was completed by adding a 3D plot group and creating an equation from the simulation results and predefined material characteristics (for μ).

4.2 Results

Image Clarity

The collected DCE-MRI images were inspected for clarity to determine the success of the hydrogel fill and ensure fidelity of the data for later analyses (Figure 4.5. One of the Voronoi scaffolds is depicted in Figure 4.5a large gap (black cavity) throughout the majority of the scaffold, which is the result of a large air pocket in the center of the scaffold. This issue was present in all MRI imaged scaffolds, with varying degrees of severity. The IsoTruss scaffold had small central air pockets; however, they were much less severe than the air pockets in the Voronoi scaffolds. Within the IsoTruss image data, there were MRI image slices of the hydrogel-filled scaffold that were uninterrupted by the presence of air. For these slices, the struts of the IsoTruss scaffold were clearly visible across the image, represented

by the black/dark grey lines. For all captured MRI-images, the lighter gray/white regions demonstrate areas where the gadolinium contrast had illuminated the photoHA/collagen hydrogel as it flowed through or around the scaffolds.

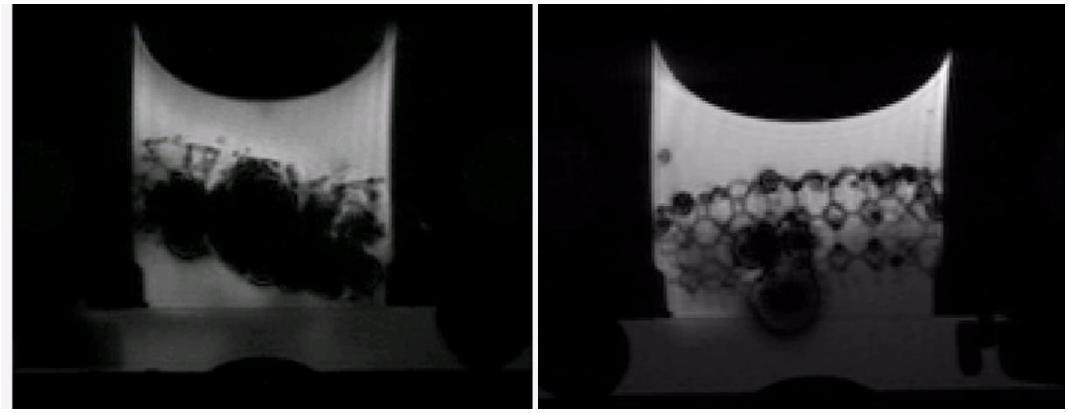

Figure 4.5: Voronoi (left) and IsoTruss (right) MRI scans.

After sitting in the desiccator, the scaffolds filled via the desiccator method had clear air pockets still remaining in the structures that were visually noticeable. Because of this, additional imaging was not necessary to evaluate this procedure. Pouring and agitating the hydrogel and scaffolds was not adequate for properly filling the scaffolds, and the desiccator was not able to remove the air.

Brightfield and DAPI scans of the scaffolds filled using the pressure differential approach revealed uniform filling with no aggregate small or large bubble clusters for any geometry (Figure 4.6). In the brightfield scans, the lighter gray regions match up with the blue stained regions on the DAPI scans, confirming that the lighter regions represent scaffold struts in the brightfield scans. The black specs that are clearly visible in the DAPI scans represent small/micro-air bubbles present in the gelatin hydrogel. This trapped air is a product of the hydrogel production method, confirmed by their homogenous distribution throughout the scaffolds, and do not represent a failure of the filling method. Moreover, these micro-air bubbles do confirm that in the DAPI scans, air pockets would be represented by large black spots. The various scans do not show evidence of large air pockets created as a result of the

hydrogel not fully penetrating throughout the scaffold and into each pore. The scans confirm that the pressure differential method successfully eliminated air pockets in the three geometries tested and imaged.

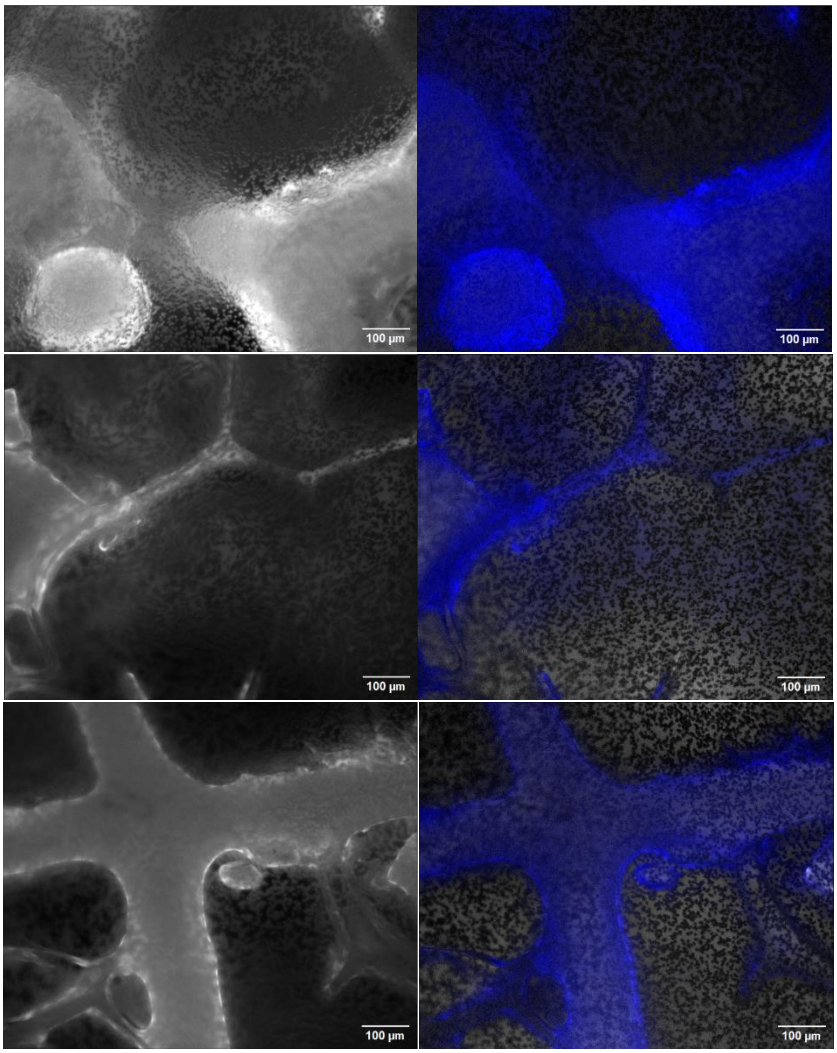

Figure 4.6: Example brightfield (left) and DAPI (right) echo microscope scans of IsoTruss (top), Truncated Octahedron (middle), and Voronoi (bottom) scaffolds with gelatin hydrogel fill via pressure differential method. Light gray regions on the brightfield scans represent scaffold struts, and blue regions on the DAPI scan represent scaffold struts.

DCE-MRI Direction and Velocity

Due to the air pockets in both Voronoi samples subjected to DCE-MRI imaging, only the sequential DCE-MRI images of the IsoTruss scaffold were included for further assessments. The DCE-MRI analysis produced direction and velocity vector fields, representing the movement of gadolinium

contrast through the scaffold. Because of the presence of air pockets, it was difficult to discern what movement was a result of air pocket/bubble displacement and what movement was due to the scaffold geometry. Despite this, the velocity streamlines (magnitude) and velocity direction were computed for an entire IsoTruss 2D slice (Figure 4.7.

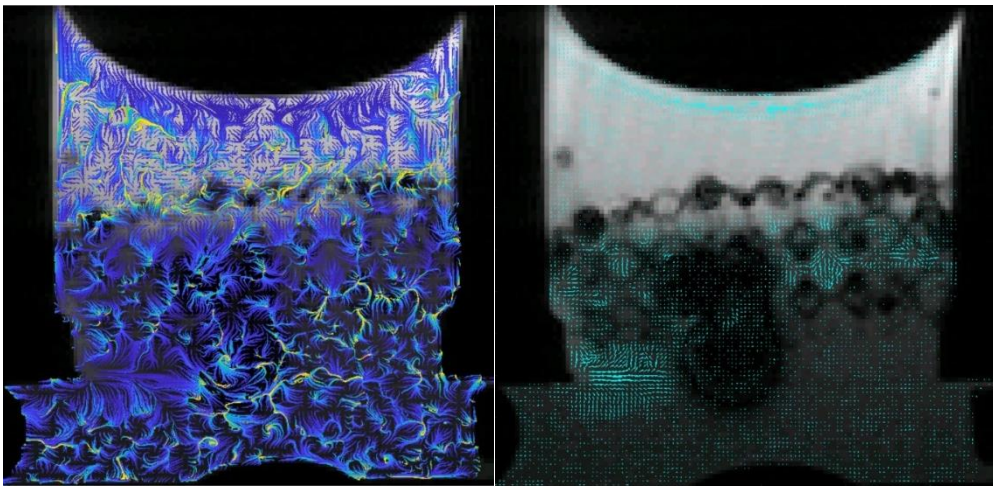

Figure 4.7: 2D MRI image slices overlayed with velocity streamlines (left) and direction streamlines (right) within a IsoTruss scaffold undergoing diffusion flow (infusion rate of 500 µL/min)

Because of the relatively larger scale of the scaffold and hydrogel, the median velocity and direction quantitative data for the whole scaffold does not reveal much about the movement of fluid throughout the geometry. For more relevant data, an independent analysis was performed on a portion of the scaffold representing a unit cell of the IsoTruss scaffold (Figure 4.8). The average velocity in this portion was 0.689 µm/s, and the average direction of flow was 168°. The magnitude of velocity was higher at the top portion of the diagonal strut, while velocity was near the intersection of the two pictured struts at the bottom of the diamond shape.

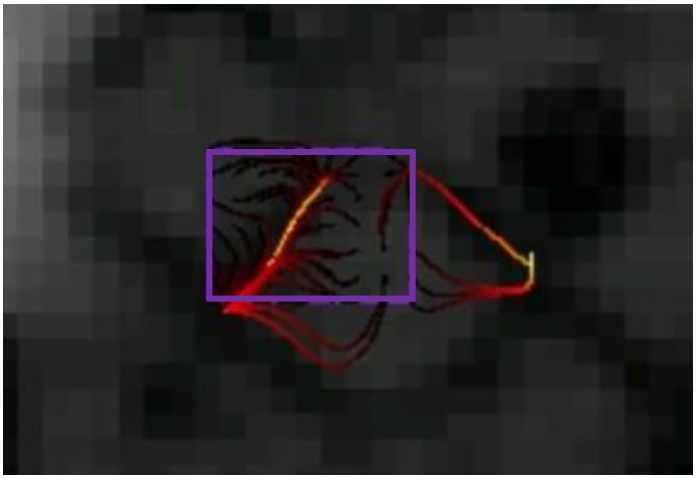

Figure 4.8: DCE-MRI streamline analysis of single unit geometry slice. The purple box outlines the region involved in the analysis, which is one unit cell of the IsoTruss geometry. Yellow/brighter regions indicate higher velocity; whereas, red/darker regions indicate lower velocity.

COMSOL Velocity Direction and Magnitude Calculations

Pictured in Figure 4.9 and 4.10 are the graphed results of the simulation at an inlet velocity of 0.15 mm/s. According to this simulation, depicted in Figure 4.9A and 4.10A, velocity is greatest towards the center of the pores, and around the strut when flow is coming from the top and being divided around the strut. A bias towards the left side is seen in the bottom images in which a side inlet boundary is introduced. Additionally, a greater maximum velocity is achieved in the simulation with two inlet boundaries.

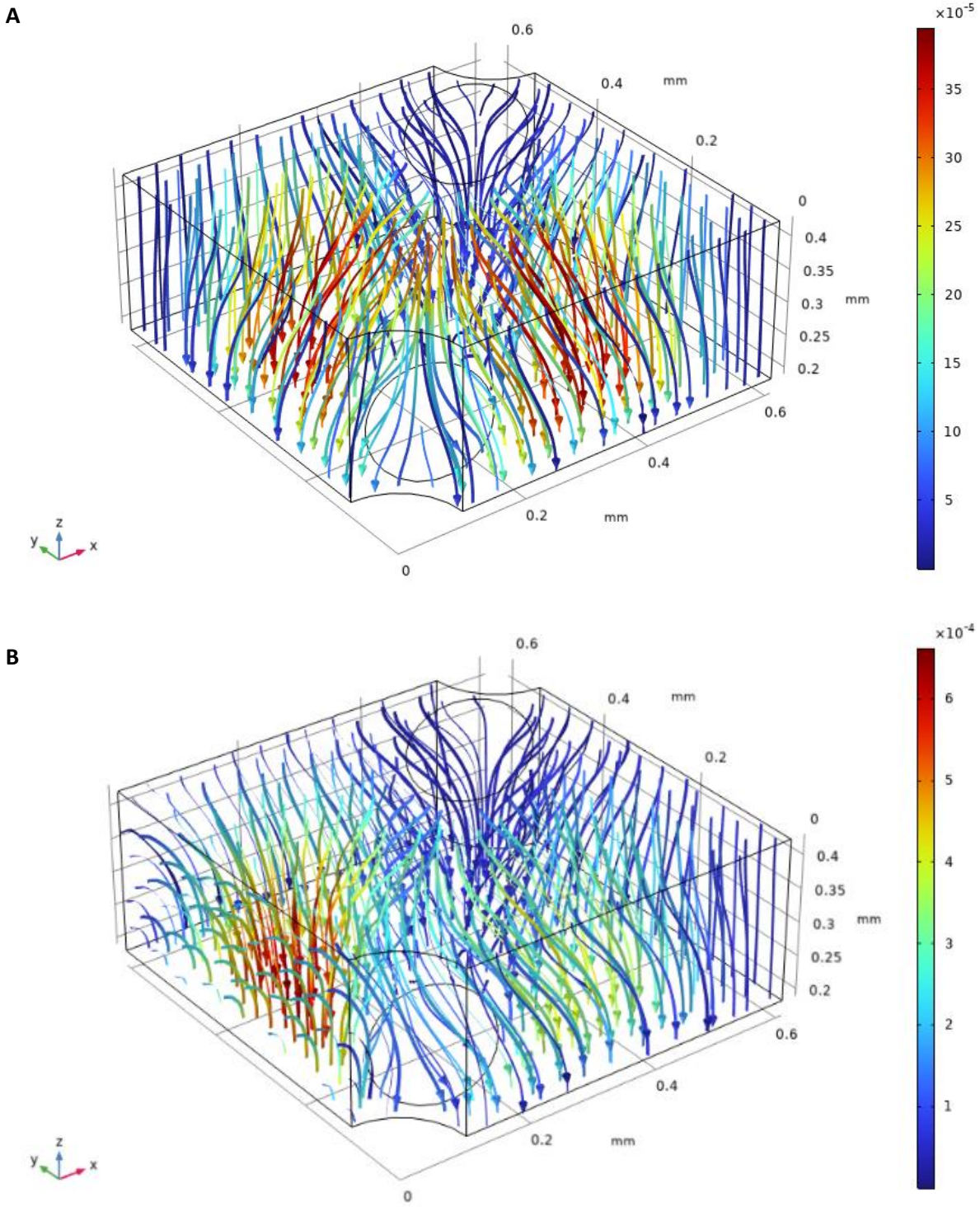

Figure 4.9: Velocity direction field streamlines of IsoTruss scaffold slice with an inlet velocity of 0.15 mm/s coming from top boundary (A) and top and front left boundary (B). Note, the scale bars have different magnitudes, but the same color scale.

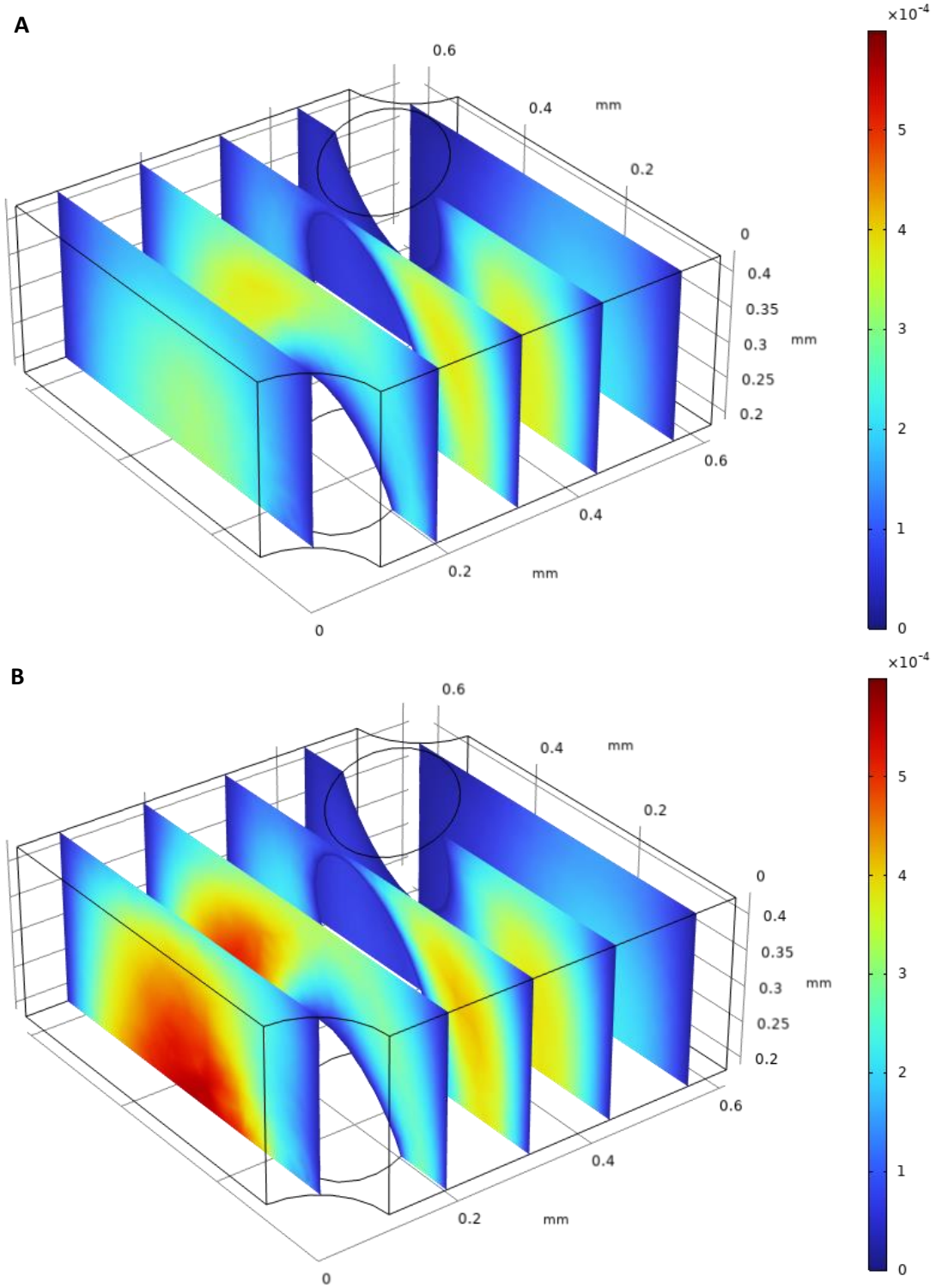

Figure 4.10: Velocity magnitude map in slices of IsoTruss scaffold slice with an inlet velocity of 0.15 mm/s coming from top boundary (A) and top and front left boundary (B).

Wall Shear Stress Surface Calculation

Figure 4.11 represents the WSS surface calculation for a central, diagonal strut in the IsoTruss scaffold. This simulation was able to successfully complete the calculation, and graphically represent the results on the surfaces of the imported geometry. The slowest inlet velocity (0.05 mm/s) produced a maximum WSS of about 8.5 mPa; whereas, the fastest inlet velocity (0.25 mm/s) produced a maximum WSS almost 5x greater than that of the slowest. The introduction of an inlet boundary on the side surface did not appear to have an impact on the magnitude of WSS produced on the central strut.

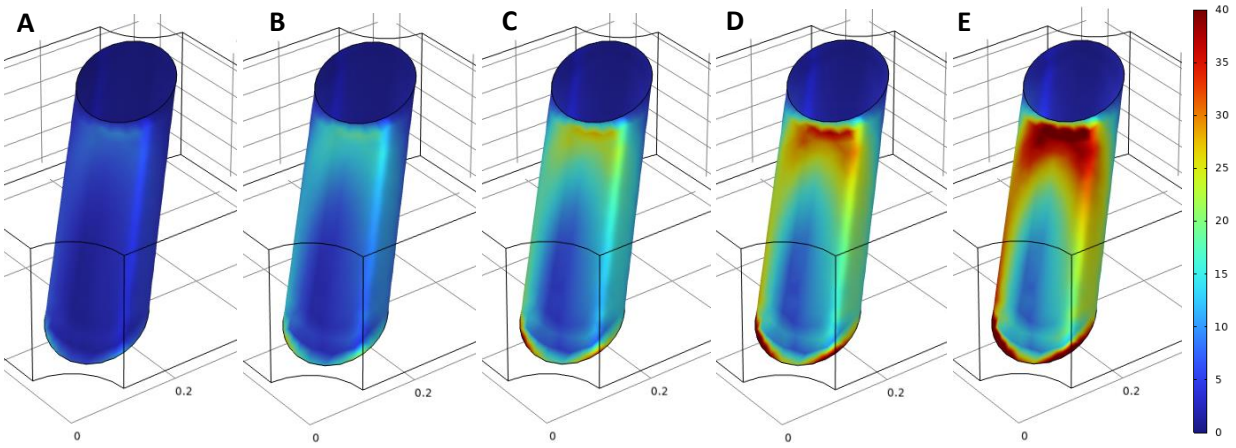

Figure 4.11: Surface WSS (mPa) map for central IsoTruss unit geometry slice at various inlet velocities (mm/s): A) 0.05 mm/s; B) 0.10 mm/s; C) 0.15 mm/s; D) 0.20 mm/s, and; E) 0.25 mm/s. The scale bar is consistent for each WSS map.

4.3 Discussion

This study achieves several objectives that had not been previously accomplished: 1) DCE-MRI was performed and used to analyze fluid flow through complex geometries for the first time; 2) sample preparation was optimized to ensure even distribution of hydrogel throughout the three scaffold geometries; and 3) a CFD model of an IsoTruss unit cell was developed that replicates patterns observed in experimental DCE-MRI fluid flow analysis.

The DCE-MRI analysis confirms that this methodology can be adapted to hydrogel-filled scaffolds in order to collect velocity and direction data. Up to this point, DCE-MRI has not been performed on a 3D

rigid structure with distinct microstructural features, making this study the first step in developing a protocol and collecting preliminary data for future works. The imaging of the scaffolds visually represents how the introduction of a scaffold structure to a hydrogel manipulates the movement of particles through the transwell, and the velocity direction and magnitude plots reveal insights of the internal structures of the scaffolds that were previously unknown.

The additional analysis on the smaller region of the scaffold reveals more relevant insights that impacted decisions made in the CFD simulation. At the corner intersection/node, there are fourteen struts meeting at one point, which creates a bottlenecking effect that could explain the observation of slower fluid flow at the bottom half of the diagonal strut. The other geometries do not have intersections with this much activity, so these large intersection points have an impact on the velocity magnitude and direction. Another important insight this analysis reveals is that fluid moves towards the diagonal strut from the center of the pore, and not just from the top. Again, this is most likely due to the modified movement required to get around the thick intersection points. This observation became important during the CFD analysis in selecting the inlet flow boundaries. Rather than having flow move from the top to bottom boundary, considerations were made to investigate the impact of flow from multiple directions. The outlet boundary remained constant for both simulations because the DCE-MRI data did not conclusively reveal if fluid was moving out of the region in any direction other than downward. When compared to the DCE-MRI results, the velocity magnitude and direction from the COMSOL simulation was more realistic when flow came from more than one direction. In such a complex structure, it is difficult to make assumptions about where the flow comes from in such a small unit geometry, which highlights the importance of imaging techniques in better understanding complex structures and flow mechanics.

This simulation reveals important insights on the selection of inlet velocities for a perfusion bioreactor system in future studies. WSS from 0.55 mPa to 24 mPa can induce the formation of ECM from bone cells[21], and the inlet velocity that best achieves this range is 0.15 mm/s. For comparison, some inlet velocities used in other fluid-induced WSS studies are 0.4 mm/s[22], 0.5 mm/s[21], and 1 mm/s[19], with a higher extreme being 61 mm/s[19]. Because this simulation only achieves the higher range of WSS for ECM formation in one small region of the strut, a higher inlet velocity could be justified to achieve higher WSS on more surface area. A limitation of the CFD analysis was that the complex geometries could not be completely replicated in the COMSOL software, and creating a modifiable replica of the geometry was a challenge. While the CFD analysis is limited by the MultiPhysics capabilities in the COMSOL software, the impact that changing the inlet boundaries has on the flow velocity vectors does reflect how making modifications based on collected data are able to improve the results.

The original goal of Aim 2 was to develop a validated computational model that simulates fluid flow and optimizes WSS within an organoid. The completed COMSOL CFD analysis effectively calculates WSS on a IsoTruss scaffold unit cell, accounting for resin material properties, fluid properties, and varied inlet velocities. While the validation data is sparce due to MRI machinery maintenance and repairs, the developed CFD model was validated against experimental DCE-MRI data, confirming the utility of the *in silico* model at recapitulating the *in vitro* model conditions. While the work done outlined in this chapter provides a platform for validating a computational model, limitations in the experimental data collection process and computational bandwidth pivoted my research into focusing on protocol development rather than validation of full-size IsoTruss, Voronoi, and Truncated Octahedron scaffold CFD simulation data. As the first person collecting this type of data for the three scaffolds being analyzed, I was able to lay a foundation for a more complete analysis with access to more resources.

This protocol development involved hydrogel formula and filling optimization. Several types of hydrogels were explored in this thesis to fill porous 3DP scaffolds. The hydrogel made from the gelatin from porcine skin performed best for this procedure as it did not require photocuring nor does it contain collagen. The photo curing required for the photoHA/collagen hydrogel could impact the mechanical properties of the scaffolds, as they are photo cured in the fabrication process. Despite the benefits of using the porcine skin hydrogel, several challenges persist regarding preparation of the material: (1) the gelatin sets quickly, so it is important that the scaffold samples are prepared and ready as soon as the hydrogel comes off of the stir plate; (2) the method for preparing this hydrogel introduces homogenously distributed micro-bubbles (Figure 4.6). Future studies should explore available methods for eliminating these air bubbles to further optimize the hydrogel prep and filling procedure.

The pour over method for filling the scaffolds, as demonstrated by the MRI scans, was clearly inadequate for the complex scaffold geometries included in this thesis; further, the added pressure of a vacuum desiccator was insufficient to clear air bubbles from the scaffolds. With such intricate architectures, more pressure and agitation were needed to fully integrate the hydrogel to all pores of the scaffold. The desiccator method procedure could have been limited by the fact that the wells that the scaffolds were sitting in were too big for the scaffold slices. Originally, I thought that if the scaffolds were submerged with hydrogel in a larger well, it would help to fill out the pores from more directions than just the top; however, it seems like the hydrogel traveled away from scaffold rather than into it. There was no evidence of air pockets in any of the scans taken of the scaffolds using the pressure differential method, indicating that all air bubbles created as a result of filling pore space were extracted through the permeable membrane. The transwell inserts used in DCE-MRI with the permeable bottom surface allows for this process to be successful, as pulling air through the bottom is the best technique for

extraction. This technique also requires minimal resources that are inexpensive and reusable, allowing for the procedure to be performed accessibly in the future.

Chapter 5: Conclusion

5.1 Synthesis

This master's thesis describes the development of a pipeline for analyzing ECM formation and mineralization in 3D printed scaffold via dynamic mechanical analysis (DMA) and computational fluid dynamics (CFD). Further, proof-of-concept validation data was generated using dynamic contrast-enhanced MRI (DCE-MRI), confirming that fluid flow velocity and direction data can in fact be collected on hydrogel-embedded stiff scaffold structures. Three scaffold geometries—Voronoi, IsoTruss, and Truncated Octahedron (TO)— were investigated for their utility in fracture healing research, yielding robust structural and mechanical (storage modulus, loss modulus, and tan delta) characterization data. Finally, the COMSOL simulation-validated DCE-MRI data generated within this thesis will be critical for characterizing the velocity magnitude and direction of flow within future scaffolds, as well as in the optimization of the wall shear stress (WSS).

Not only does this thesis provide a pipeline for mechanical characterization of the scaffolds but it also provides initial insights into how the scaffold geometries compare in terms of mechanical stiffness following cell culture. There is a wide range of storage moduli of trabecular bone fracture callus, and the average stiffnesses of the scaffolds were at the bottom of this range. Voronoi samples were significantly stiffer when seeded for seven days compared to four days, and the presence of cells in the scaffolds did have a significant impact on storage modulus. The IsoTruss scaffold absorbed and dissipated energy much differently than the Voronoi and TO scaffolds, as demonstrated by the higher average damping coefficient. This suggests a possible buckling movement occurring within the scaffold, which the micromechanical analysis through DCE-MRI and CFD could give more insight on in future studies. More samples need to be tested to validate these findings, but they serve as a good starting point for scaffold comparison.

I was able to work around the complex IsoTruss geometry by creating my own slices of a unit cell of the scaffold in order to simulate WSS on a characteristic strut within a pore of the IsoTruss scaffold. The resulting WSS was a result of a realistic inlet velocity of fluid that simulates perfusion through a bioreactor. This validated model can be used in future cell culture experiments to optimize fluid flow and WSS through these geometries.

Though impactful, the preliminary DCE-MRI data collected is not publishable due to air pockets in the hydrogel-filled scaffolds. Motivated by this challenge, I developed an SOP to prepare scaffolds for imaging in a way that eliminates air pockets and processed the collected data to serve as proof-of-concept for future studies. As a result, velocity direction and magnitude data were acquired for the IsoTruss geometry. Up to this point, DCE-MRI imaging has only been done on hydrogels, making this the first set of collected DCE-MRI data on a rigid structure. On the large scale of the scaffold, there are detectable patterns that seem to be true throughout the scaffold. For example, fluid moves from the center of the pores towards the struts, and as it flows down the strut there is apparent bottlenecking at the intersection of struts. This points out a possible limitation of the IsoTruss scaffold that is consistent with the DMA results and overall scaffold observations. This scaffold is the only geometry in which at each internal intersection, fourteen struts meet at one point. This creates large “knots” in the structure, where fluid flow is slowed down. This micromechanical observation confirms the higher tanδ values for IsoTruss calculated through DMA testing and with this closer look at the scaffold, our original explanation of buckling is supported. Additionally, the IsoTruss scaffold is the only geometry in which consistent printing fidelity issues are observed. For each scaffold within the tested IsoTruss groups (four-day seeded, seven-day seeded, four-day soaked, seven-day soaked) there has consistently been one scaffold in each group that is much stiffer than the others. The crowded intersections/nodes in this scaffold may create fidelity problems, necessitating stricter fabricating and curing parameters to produce consistent

scaffolds than the other geometries. The DCE-MRI data that was analyzed for just a small portion of the scaffold became important in determining where flow comes from in the COMSOL simulation. When the inlet boundaries were changed to better fit the data found in the DCE-MRI analysis, the results of the simulation became much more realistic and consistent with the DCE-MRI data.

As a response to the problems observe in collecting DCE-MRI data, I developed protocol that will avoid these problems in the future. Although a simple concept, the pressure differential method I created using a syringe and tubing around the transwell insert was very successful at eliminating air pockets in the scaffolds. This method will be incorporated into the sample preparation process in the future when collecting DCE-MRI or DCE-CT data.

5.2 Future Work

The immediate next steps for this project are DCE-MRI sample prep and data collection for all three scaffold geometries. This will involve performing the pressure differential scaffold filling technique on cylindrically printed scaffolds with 12.5 mm diameters. Additionally, more IsoTruss samples should be printed, seeded, and DMA tested for four- (n=2) and seven-days (n=2) so that each group has the same sample size.

5.2.1 Fracture Healing Prediction

For the Bone Organoid project, these two aims I completed are just the beginning of a long-term study that will investigate delayed fracture healing on an individual patient basis. The project is motivated by the fact that current clinical practices and imaging techniques do not reliably assess the patient risk of experiencing delayed fracture healing or nonunion. The goal is to explore an *in vitro* option for analyzing individual capacity for bone healing—the bone organoid. The three scaffold geometries—IsoTruss, Voronoi, and TO—will be the foundation from which to expand the organoid

development, and the preliminary data I collected will inform decisions moving forward with these structures.

There is yet to be a bone organoid developed that effectively recapitulates the complex micromechanical environment of bone. Additionally, mechanosensitivity cell markers, which could be critical in understanding individual bone healing capacity, have not been identified. The bone organoid we have begun to develop aims to address these gaps in knowledge and allow for a platform that can be mechanically stimulated and micromechanically studied. The objective of this larger project is to induce strain stimulated ECM formation and develop mineralized tissue in an environment in which it can be quantitatively measured. With this system, steps can be made towards patient-tailored treatment plans to intervene early on delayed fracture healing and nonunion.

5.2.2 Bone to Breast Metastasis

Another application of the bone organoid in development is in the study of metastatic breast cancer. A common site where breast cancer metastasizes is bone; however, this migration of cancer cells is not completely understood. Characteristics of cancer cells that increase survival and proliferation have not been linked to bone metastases. Studying the interaction of cancer cells with ECM formed in a bone organoid could reveal insights as to why the cancer commonly metastasizes there. The *in vitro* environment provided by a bone organoid allows for the study of cancer cell interaction with bone cells to identify how glycosylation impacts mechanical characteristics of the organoid. This future study could provide insights that lead to potential therapies for metastatic breast cancer, improving the lives and outcomes for patients.

References

1. Cheng HH, Carmona F, Mcdavitt E, et al. Fractures Related to Metabolic Bone Disease in Children with Congenital Heart Disease. Congenit Heart Dis. 2016;11(1):80-86. doi:10.1111/CHD.12293
2. Roddy E, Debaun MR, Daoud-Gray A, et al. Treatment of critical-sized bone defects: clinical and tissue engineering perspectives. European Journal of Orthopaedic Surgery & Traumatology. 2018;28:351-362. doi:10.1007/s00590-017-2063-0
3. Schemitsch EH. Size Matters: Defining Critical in Bone Defect Size! J Orthop Trauma. 2017;31:20-22. doi:10.1097/BOT.0000000000000978
4. Schlundt C, Bucher CH, Tsitsilonis S, Schell H, Duda GN, Schmidt-Bleek K. Clinical and Research Approaches to Treat Non-union Fracture. Curr Osteoporos Rep. 2018;16(2):155-168. doi:10.1007/S11914-018-0432-1/TABLES/2
5. Hak DJ, Fitzpatrick D, Bishop JA, et al. Delayed union and nonunions: Epidemiology, clinical issues, and financial aspects. Injury. 2014;45(SUPPL. 2):S3-S7. doi:10.1016/J.INJURY.2014.04.002
6. Catalano E, Cochis A, Varoni E, Rimondini L, Azzimonti B. Tissue-engineered skin substitutes: an overview. Journal of Artificial Organs. 2013;16:397-403. doi:10.1007/s10047-013-0734-0
7. Zadpoor AA. Biomaterials Science REVIEW Bone tissue regeneration: the role of scaffold geometry. Biomater Sci. 2015;3:231. doi:10.1039/c4bm00291a
8. Bidan CM, Kommareddy KP, Rumpler M, Kollmannsberger P, Fratzl P, Dunlop JWC. Geometry as a Factor for Tissue Growth: Towards Shape Optimization of Tissue Engineering Scaffolds. Adv Healthc Mater. 2013;2(1):186-194. doi:10.1002/ADHM.201200159
9. Moroni L, De Wijn JR, Van Blitterswijk CA. 3D fiber-deposited scaffolds for tissue engineering: Influence of pores geometry and architecture on dynamic mechanical properties. Biomaterials. 2006;27(7):974-985. doi:10.1016/J.BIOMATERIALS.2005.07.023
10. Novosel EC, Kleinhans C, Kluger PJ. Vascularization is the key challenge in tissue engineering. Adv Drug Deliv Rev. 2011;63(4-5):300-311. doi:10.1016/J.ADDR.2011.03.004
11. Chartrain NA, Williams CB, Whittington AR. A review on fabricating tissue scaffolds using vat photopolymerization. Acta Biomater. 2018;74:90-111. doi:10.1016/J.ACTBIO.2018.05.010
12. Huang J, Zhang L, Lu A, Liang C. Organoids as Innovative Models for Bone and Joint Diseases. Cells. 2023;12(12):1590. doi:10.3390/CELLS12121590
13. Duan Z wei, Lu H. Effect of Mechanical Strain on Cells Involved in Fracture Healing. Orthop Surg. 2021;13(2):369-375. doi:10.1111/OS.12885
14. Chen JC, Jacobs CR. Mechanically induced osteogenic lineage commitment of stem cells. Stem Cell Res Ther. 2013;4(5):1-10. doi:10.1186/SCRT318/FIGURES/3
15. Gibbs JC, McArthur C, Wark JD, et al. The Effects of Home Exercise in Older Women With Vertebral Fractures: A Pilot Randomized Controlled Trial. Phys Ther. 2020;100(4):662. doi:10.1093/PTJ/PZZ188
16. Flowers DW, McCallister E, Christopherson R, Ware E. The Safety and Effectiveness of Early, Progressive Weight Bearing and Implant Choice after Traumatic Lower Extremity Fracture: A Systematic Review. Bioengineering. 2022;9(12). doi:10.3390/BIOENGINEERING9120750/S1
17. Lancaster MA, Huch M. Disease modelling in human organoids. Dis Model Mech. 2019;12(7). doi:10.1242/DMM.039347

18. Leong PL, Morgan EF. Measurement of fracture callus material properties via nanoindentation. Acta Biomater. 2008;4(5):1569-1575. doi:10.1016/J.ACTBIO.2008.02.030
19. Vetsch JR, Betts DC, Müller R, Hofmann S. Flow velocity-driven differentiation of human mesenchymal stromal cells in silk fibroin scaffolds: A combined experimental and computational approach. PLoS One. 2017;12(7). doi:10.1371/JOURNAL.PONE.0180781
20. Kingsmore KM, Vaccari A, Abler D, et al. MRI analysis to map interstitial flow in the brain tumor microenvironment. APL Bioeng. 2018;2(3):31905. doi:10.1063/1.5023503/1061252
21. Zhao F, Melke J, Ito K, van Rietbergen B, Hofmann S. A multiscale computational fluid dynamics approach to simulate the micro-fluidic environment within a tissue engineering scaffold with highly irregular pore geometry. Biomech Model Mechanobiol. 2019;18(6):1965-1977. doi:10.1007/S10237-019-01188-4/FIGURES/13
22. Papadimitropoulos A, Martin I. A 3D in vitro bone organ model using human progenitor cells. Eur Cell Mater. 2011;21:445-458. doi:10.22203/eCM.v021a32

Appendix

Appendix A: SB^3C Abstract

This abstract, in which I am the first and presenting author, was accepted on April 1, 2024 for an oral presentation at the 2024 Summer Biomechanics, Bioengineering, and Biotransport Conference (SB^3C). SB^3C will take place in Lake Geneva, Wisconsin on from June 11-14, 2024

Abstract title: Dynamic micromechanical characterization of 3D printed bone *in vitro* models manufactured via vat photopolymerization

SB³C2024
Summer Biomechanics, Bioengineering and Biotransport Conference
June 11-14, Lake Geneva, WI, USA

DYNAMIC MICROMECHANICAL CHARACTERIZATION OF 3D PRINTED BONE IN VITRO MODELS MANUFACTURED VIA VAT PHOTOPOLYMERIZATION

Elizabeth A Hunt (1), S. Choi (2), E. Shangin (1), E. Nguyen (1), Dr. A. Whittington (3,4,5), Dr. C.J. Collins (1)

(1) Department of Biomedical Engineering and Sciences, Virginia Tech, Blacksburg, Virginia, USA
(2) Department of Biological Sciences, Virginia Tech, Blacksburg, Virginia, USA
(3) Department of Chemical Engineering, Virginia Tech, Blacksburg, Virginia, USA
(4) Department of Materials Science and Engineering, Virginia Tech, Blacksburg, Virginia, USA
(5) Department of Macromolecular Science & Engineering, Virginia Tech, Blacksburg, Virginia, USA

INTRODUCTION

Nonunion or delayed fracture healing is a prevalent clinical complication with a devastating impact on patient quality of life, leading to significant financial burden for patients[1]. Despite knowledge of the mechanobiology behind bone healing, we lack the ability to discern bone healing capacity in individual patients. Existing biomarkers for healing progression and clinical imaging modalities fail to discern which patients experience delayed fracture healing or proceed to nonunion. Current preclinical models for bone fracture healing rely on 2D cell culture and animal experiments, each with their own limitations regarding translation to patients[2]. Additionally, current detection strategies such as radiolucency in planar x-rays and reported pain by the patients do not account for the *in vivo* mechanical environment[3,4] though studies have shown a positive relationship between loading and bone healing[5]. 3D culture systems such as organoids provide an *in vitro* tissue culture platform that allow for the prolonged study of human cells in an environment that mimics *in vivo*[6]. To develop such a platform for assessing individual patient risk factors for non-union, this study aims to manufacture porous 3D scaffold geometries using a novel, osteoconductive resin via vat photopolymerization (VP) and analyze their ability to mimic the *in vivo* bone micromechanical environment.

METHODS

Resin Formulation: A mixture of 50 wt% epoxidized soybean oil acrylate (ESOA, Sigma-Aldrich) and 50 wt% polyethylene glycol diacrylate (PEGDA, Sigma-Aldrich, MW = 575) was used to formulate the resin for printing. To promote curing, 1 wt% diphenyl(2,4,6-trimethylbenzoyl)phosphine oxide photoinitiator (Sigma-Aldrich) and 0.20 wt% 2,5-bis(5-tert-butyl-benzoxazol-2-yl)thiophene UV absorber (TCI Chemicals) was added.

Scaffold Printing & Sterilization: Three scaffold geometries (Voronoi, IsoTruss, and Truncated Octahedron (TO)) were designed (nTopology, Figure 1) with 489, 476, and 554 µm average pore diameters, respectively, and printed using a VP bottom-up platform (Autodesk Ember). Five burn-in layers underwent UV exposure (5 W, λ = 405 nm) for 25 s per layer, and the rest of the model layers were exposed for 2.5 s per layer. Every layer was 0.1 mm thick for a total of 10 mm for the entire scaffold. After printing, the burn-in layers were removed and the scaffolds were washed in 70% isopropyl alcohol (IPA) and UV cured for one minute.

Prior to cell seeding, scaffolds underwent sterilization using 70% ethanol for 1 hr, followed by 3 washes with phosphate buffered saline (PBS) and a final wash using media made of αMEM and supplemented with 10% fetal bovine serum (FBS) and 1% penicillin-streptomycin-amphotericin (Thermo-Fisher).

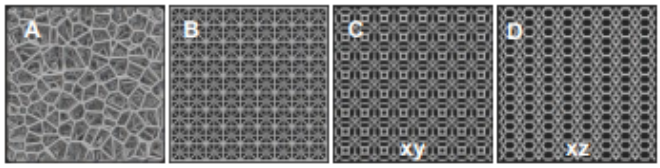

Figure 1: Voronoi (A), IsoTruss (B), and TO (C & D) lattices.

Cell Seeding & Analysis: Murine fibroblasts (1 x 10^5 NIH 3T3) were seeded on each scaffold (n = 6/geometry) and cultured in media under static conditions for 4 and 7 days, with media exchange every 2-3 days. Subsequently, each sample was immersed for 5 minutes in 1 mL 10% formalin fixation solution, rinsed with PBS, and immersed in 1 mL of a post-fixation solution of 10% formalin. Scaffolds were then rinsed in PBS for 1 minute and stained with DAPI and Rhodamine Phalloidin dyes (Thermo-Fisher) for 1 hr in the dark before storage in deionized water at 4°C.

For assessment of the structural fidelity and biocompatibility, the scaffolds were cut in half and examined using a laser scanning confocal fluorescence microscope (Zeiss Axio Observer.Z1) with 10x objective (Plan-Apochromat 10x/0.45 M27, Zeiss) and 60 µm diameter pinhole.

Consistent processing and analysis of image stacks (voxel size 0.85x0.85x5.4 µm) were employed to assess cell nuclei spatial distribution within the scaffolds and the pore distribution within the scaffolds following image segmentation (ImageJ).

Dynamic Mechanical Analysis: Dynamic mechanical analysis (DMA, ElectroForce 3200) was performed on the seeded (n=6/geometry/day culture) and unseeded (n=1/geometry) scaffolds via cyclic compression using a strain sweep to analyze how microstructure impacts the organoid elastic modulus (E', storage modulus), viscous modulus (loss modulus), and damping coefficient (tanδ). The strain sweep was conducted at a frequency of 0.1 Hz starting with a dynamic amplitude of 0.2 mm (4% strain) and increasing by 0.1 mm until reaching 1 mm dynamic amplitude (10% strain). All testing was performed submerged in a 1x concentrated phosphate-buffered saline (PBS, pH 7.4) solution at 37 °C.

Statistical Analysis: Mechanical data was analyzed for descriptive statistics (python) using paired t-tests to determine significant differences between the 4-day and 7-day cultured scaffolds (α=0.05).

RESULTS

After 4 and 7 days of seeding, confocal microscopy confirmed successful cell adhesion and proliferation, with cells well distributed throughout all three scaffold geometries (Figure 2). Average pore diameters were 579, 397, 662 µm for the Voronoi, IsoTruss, and TO scaffolds, respectively, within range of the targeted print size.

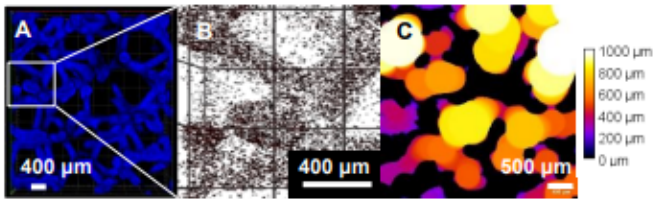

Figure 2: Voronoi structure (A, DAPI), cell nuclei distribution (B, Rhodamine), and pore thickness distribution map (C).

Some of the IsoTruss scaffolds (n=2) failed prematurely during the DMA testing due to inconsistencies in the printing, these were excluded from further analyses. For the remaining scaffolds, average storage modulus increased from day 4 to 7 of static culture (Table 1). The stiffest storage modulus achieved overall was reached by a 7-day cultured IsoTruss scaffold (2.70 MPa) Note, variation in the storage modulus for the 7-day IsoTruss scaffolds was the highest. The Voronoi scaffolds had the only significant and consistent increase in storage modulus between 4- and 7-day cultures (p=0.0293).

Table 1: Storage modulus (MPa) of the three scaffold geometries for 4- and 7-day cultures (mean ± SD).

Day	n	IsoTruss	TO	Voronoi
0	1	1.08	0.46	0.91
4	6	0.80±0.53*	0.64±0.40	0.55±0.25
7	6	0.81±1.27*	0.69±0.35	1.19±0.57
*n=4 for IsoTruss 4- and 7-day culture mechanical testing				

The peak storage modulus for the Voronoi 7-day cultured scaffolds is 2.26 MPa. Both of these peaks for IsoTruss and Voronoi are reached at the first strain sweep condition of 2% strain, or a dynamic amplitude of 2 mm. The peak storage modulus is achieved by a 4-day cultured scaffold for the TO geometry at 1.28 MPa at 2.14 % oscillation strain. Trends in loss modulus were consistent among the Voronoi and TO scaffolds, with a general increase with increased oscillation strain (Figure 3). On average, the loss modulus of IsoTruss scaffolds decreased at higher oscillation strains, leading to a tanδ of 0.0613, which is over 2x greater than Voronoi (0.0227) and TO (0.0297) at 2% strain.

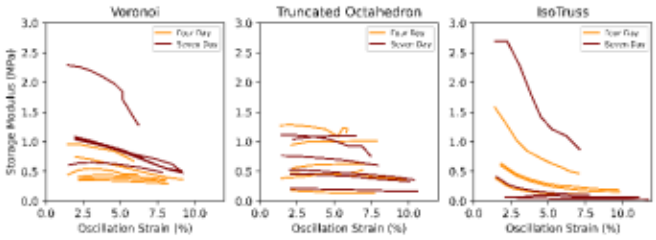

Figure 3: Storage modulus (MPa) vs. oscillation strain (%) for Voronoi, TO, and IsoTruss scaffolds.

DISCUSSION

Scaffold stiffness varied, with storage moduli on the order of soft fracture callus tissue after seeding (fracture callus moduli: 0.5-1000 MPa)[7]. Despite the limited number of samples available for testing, trends were observed on how seeding impacted scaffold stiffness. IsoTruss scaffolds achieved the maximum storage modulus of all 7-day seeded scaffolds; however, the rest of the 7-day IsoTruss seeded samples were significantly softer than the average TO and Voronoi scaffolds. Voronoi scaffolds had more consistent mechanical properties, while still achieving the second highest value for storage modulus. Further, Voronoi scaffolds had the most consistent increase in modulus with longer culture times, which may suggest the more consistent formation of extracellular matrix. Note, however, the range between 4- and 7-day seeded Voronoi scaffold storage moduli is limited. A portion of the IsoTruss scaffolds were too soft to perform DMA testing on, which could be due to inconsistencies in either the printing parameters or the curing process. As such, the remaining IsoTruss samples may have also been impacted by the same inconsistencies that prevented testing of the rest of the samples, contributing to the significantly higher damping detected in the IsoTruss specimens. Further spatial analysis of the cell distribution may also provide insight into the differences observed between scaffold geometries and culture time. The results of this study represent a successful first step at generating an organoid that recapitulates the micromechanical environment of healing bone. The investigated scaffold geometries 3DP via VP using the novel ESOA and PEGDA resin resulted in successful cell adhesion, proliferation, and extracellular matrix deposition, providing valuable insight into the structure/function relationship of pore shape and bone organoid mechanical properties.

ACKNOWLEDGEMENTS

We acknowledge support from the Beckman Scholar Foundation and the National Center for Advancing Translational Science of the NIH Award UL1TR003015/ KL2TR003016.

REFERENCES

[1] Hak, DJ et al., *Injury*, 45:S3-S7, 2014.
[2] Huang, J et al., *Cells*, 12:1590, 2023.
[3] Chen, JC, Jacobs, R, *Stem Cell Res Ther*, 4:107, 2013.
[4] Duan, ZW and H Lu, *Orthop Surg*, 13:369–375, 2021.
[5] Flowers, DW et al., *Bioeng*, 9:750, 2022.
[6] Lancaster, MA, Hutch, M, *Dis Model Mech,* 12:039347, 2017.
[7] Leong, PL, Morgan, EF, *Acta Biomater*, 4:1569-75, 2008.

Appendix B: BMES Abstract

This abstract, in which I am the first and presenting author, was accepted to the Biomedical Engineering Society (BMES) Annual Conference on August 23, 2023 for a poster presentation. BMES took place in Seattle, Washington from October 11-14, 2023.

Abstract title: Dynamic micromechanical characterization of 3D printed bone organoids manufactured via vat photopolymerization

DYNAMIC MICROMECHANICAL CHARACTERIZATION OF 3D PRINTED BONE ORGANOIDS MANUFACTURED VIA VAT PHOTOPOLYMERIZATION

E. Hunt (1), S. Choi (2), E. Nguyen (1), Dr. A. Whittington (3,4,5), Dr. C. Collins (1)

(1) Department of Biomedical Engineering and Sciences, Virginia Tech, Blacksburg, Virginia, USA
(2) Department of Biological Sciences, Virginia Tech, Blacksburg, Virginia, USA
(3) Department of Chemical Engineering, Virginia Tech, Blacksburg, Virginia, USA
(4) Department of Materials Science and Engineering, Virginia Tech, Blacksburg, Virginia, USA
(5) Department of Macromolecular Science & Engineering, Virginia Tech, Blacksburg, Virginia, USA

INTRODUCTION

Nonunion or delayed fracture healing is a prevalent clinical complication with a devastating impact on patient quality of life. These are challenging injuries to treat and lead to significant financial implications for the patient[1]. Despite our knowledge of the mechanobiology behind bone healing, we lack the ability to discern bone healing capacity on an individual patient basis. Further, there are no routine lab tests or imaging modalities currently available that provide reliable assessment for risk mitigation of such undesired outcomes. Current preclinical models for bone fracture healing rely on 2D cell culture and animal experiments, each with their own limitations regarding translation to patients[2]. 3D culture systems such as organoids provide an in vitro tissue culture platform that allow for the prolonged study of human cells in an environment that mimics conditions in which tissue operates inside of the body[3]. In order to develop such a platform for assessing individual patient risk factors for non-union, this study aims to characterize the mechanical properties of three different 3D scaffold geometries manufactured using a novel, osteoconductive resin via vat photopolymerization (VP) and analyze their ability to mimic the microstructural environment of human bone.

MATERIALS & METHODS

Porous scaffolds (n=15, 10x10x10mm, 0.5mm avg. pore diameter) were 3D printed (3DP) via vat photopolymerization (VP, Autodesk Ember 3D Printer) with IsoTruss, Truncated Octahedron (TO), and Voronoi lattice geometries using a 50% wt. epoxidized soybean oil acrylate (ESOA) and 50% wt. polyethylene glycol diacrylate (PEGDA) resin. To confirm biocompatibility, scaffolds were seeded with 3T3 fibroblasts ($1x10^5$ cells/scaffold) and cultured for 4 (n=2/geometry) and 7 days (n=2/geometry). Cell adhesion and proliferation were visually assessed using confocal microscopy following DAPI and rhodamine phalloidin staining. Dynamic mechanical analysis (DMA, ElectroForce 3200) was performed on the seeded and unseeded (n=1/geometry) scaffolds via cyclic compression using both a frequency and strain sweep to analyze how microstructure impacts the organoid storage modulus, loss modulus, and tan(delta). The frequency sweep began at 0.1 Hz and ended at 10 Hz using a logarithmic scale and remained at a dynamic amplitude of 0.2 mm (4% strain). The strain sweep was conducted at a frequency of 0.1 Hz starting with a dynamic amplitude of 0.2 mm (4% strain) and increasing by 0.1 mm until reaching 1 mm dynamic amplitude (10% strain). All testing was performed submerged in a 1x concentrated phosphate-buffered saline (PBS, pH 7.4) solution at 37 °C. All data was analyzed for descriptive statistics and plotted using Python.

RESULTS

After 4 and 7 days of seeding, confocal microscopy confirmed successful cell adhesion and proliferation, with cells well distributed throughout all three scaffold geometries. A trend for decreasing storage moduli with increasing oscillation strain was observed for each scaffold geometry, indicating damage accumulation at elevated strain levels. At a 2% oscillation strain, the measured storage modulus ranged from 0.27 to 2.70 MPa, 0.40 to 1.28 MPa, and 0.52 to 2.26 MPa for the seeded IsoTruss, TO, and Voronoi geometries, respectively. At the same oscillation strain, the unseeded IsoTruss and Voronoi scaffolds had similar storage moduli of about 1 MPa, while the unseeded TO scaffold was lower at 0.46 MPa. Compared to the unseeded TO scaffold, the seeded TO scaffolds were consistently stiffer or as stiff at each oscillation strain percentage. In contrast, the relative stiffness of the seeded and unseeded IsoTruss and Voronoi scaffolds was less consistent.

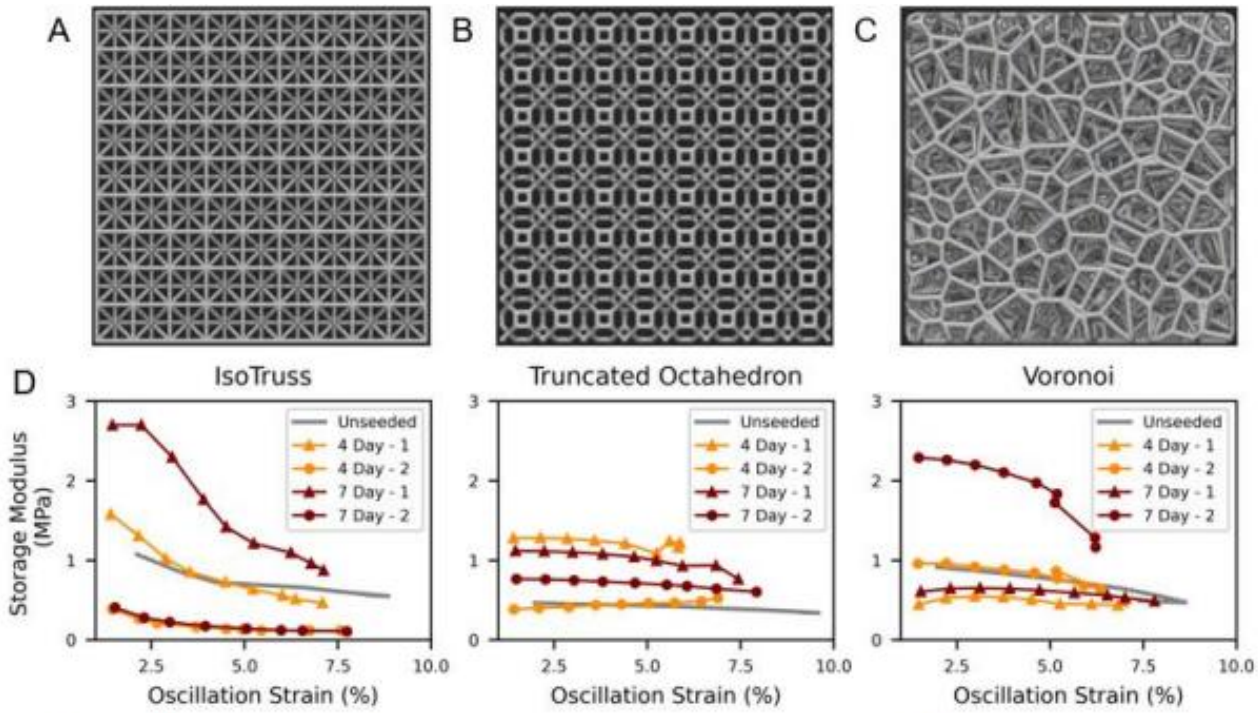

Figure 1. A) IsoTruss; B) Truncated Octahedron; C) Voronoi scaffold structures; D) Storage modulus (MPa) vs. oscillation strain (%) plots for IsoTruss, Truncated Octahedron, and Voronoi structures.

DISCUSSION

All three scaffold geometries resulted in an organoid that promoted cell adhesion and proliferation. Scaffold stiffness varied, with storage moduli on the order of soft fracture callus tissue (fracture callus indentation moduli: 0.5-1000 MPa)[4]. As such, all three geometries achieved an ideal structural stiffness prior to culture. Despite the limited number of samples available for testing, trends were observed on how seeding impacted scaffold stiffness. Following 3D culture with fibroblasts, the TO scaffolds were the only geometry to have consistently higher storage modulus. However, these scaffolds were the softest overall. Meanwhile, two-fold increases in stiffness were observed in some of the Voronoi and IsoTruss scaffolds after 7 days, suggesting substantial formation of extracellular matrix by the adherent cells. Further testing at extended culture time is needed to determine the ideal scaffold geometry for modeling bone fracture healing.

CONCLUSION

The results of this study represent a successful first step at generating an organoid that recapitulates the micromechanical environment of healing bone. The investigated scaffold geometries 3DP via VP using the novel ESOA and PEGDA resin resulted in successful cell adhesion, proliferation, and extracellular matrix deposition, providing valuable insight into the structure/function relationship of pore shape and bone organoid mechanical properties.

ACKNOWLEDGEMENTS

We acknowledge support from the National Center for Advancing Translational Science of the NIH Award UL1TR003015/ KL2TR003016 and the Beckman Scholar Foundation.

REFERENCES

[1] Hak, D. J., et al. Injury 45 (2014): S3-S7.
[2] Huang, J., et al. Cells vol. 12,12 1590. 8 Jun. 2023.
[3] Lancaster, M. A., and M. Huch. Disease models & mechanisms 12.7 (2019): dmm039347.
[4] Leong, P. L., and E. F. Morgan. Acta biomaterialia vol. 4,5 (2008): 1569-75.

Appendix C: CV

Elizabeth Hunt

Blacksburg, Virginia
elizabethhunt6@vt.edu | (757) 810-9433
www.linkedin.com/in/elizabethhunt6

EDUCATION

Virginia Tech — Blacksburg, Virginia
Bachelor of Science in Industrial & Systems Engineering, Minor in Spanish — GPA: 3.70 | May 2023
Master of Science in Biomedical Engineering — GPA: 3.71 | May 2024

EXPERIENCE

Product Development Engineer – Soft Tissue — Virginia Beach, VA
LifeNet Health — starting July 2024

- Assisting in the design, development, and maintenance of allograft manufacturing processes including improvements to existing products and processes
- Performing testing as required for research, new product/process development projects, or process improvements in compliance with Quality and Regulatory standards for allografts and medical devices

Biomedical Engineering Research Assistant — Blacksburg, VA
The Collins Lab: Hard tissue biomechanics and computational mechanobiology at Virginia Tech — January 2022 - Present

- Conducting thesis research to develop an experimental and computational pipeline for characterizing patient-specific mechanical biomarkers that indicate individual healing capacity using 3D printed bone organoids
- Collaborating and managing several projects to provide biomechanical testing and analysis
- Completing administrative tasks for the lab such as writing equipment SOPs and taking lab meeting minutes

GTA for CAD with SolidWorks (Fall) & Bioinstrumentation (Spring) — Blacksburg, VA
Biomedical Engineering and Mechanics Department, Virginia Tech — Aug 2023-May 2024

- Supporting the professor and aiding students as they need help understanding content and completing assignments
- Grading weekly lab reports and serving as a liaison between the students and professors

Product Development Design Engineering Intern — Virginia Beach, VA
LifeNet Health — Summer 2021

- Created a database for the company's custom parts over the last seventeen years
- Designed and coordinated the machining of various products for research teams
- Assisted with the biomechanical testing of an allograft bone implant
- One of the two interns awarded with a scholarship at the end of the internship out of twelve total interns

ACADEMIC HONORS & AWARDS

- Dean's List at Virginia Tech — Fall 2019 to Fall 2023
- Accepted for oral presentation at the 2024 Biomechanics, Bioengineering, Biotransport Conference (SB^3C) — June 2024

(Abstract title: Dynamic micromechanical characterization of 3D printed bone *in vitro* models manufactured via vat photopolymerization)

- Presenting Author at the Biomedical Engineering Society Annual Meeting — October 2023
  (Abstract title: Dynamic micromechanical characterization of 3D printed bone organoids manufactured via vat photopolymerization)
- Herbert H. Thompson ISE Scholarship — Fall 2021
- Pratt Engineering Scholarship — Fall 2021
- Honorable Norman Olitsky Scholarship — Fall 2021
- John S. McLellan ISE Scholarship — June 2020

INVOLVEMENT & SERVICE

- Leads lab tours for National Biomechanics Day and Women's Preview Weekend — Spring 2023, 2024
- Volunteer Young Life leader and team leader at Giles High School through Virginia Tech - responsibilities included organizing events, mentoring students, and running weekly meetings — Fall 2020 - Spring 2023
- Freshman Bible study leader — Fall 2023 - Spring 2024
- Alpha Pi Mu, Industrial and Systems Honor Society — Fall 2020 - Spring 2023
- Institute of Industrial and Systems Engineers at Virginia Tech — Fall 2020 - Spring 2023
- Biomedical Engineering Society — Fall 2023 - Spring 2024
- Service mission trip to Lima, Peru — Summer 2019
- Counselor at Camp Willow Run with the Children's Ministry from First Baptist Church of Norfolk — Summer 2018 and 2019

PROFICIENCIES

- Proficient in SolidWorks, Python, MATLAB, Microsoft Word, PowerPoint, and Excel
- Biliterate and conversationally fluent in Spanish

Appendix D: Scaffold Testing SOP

The Scaffold Testing SOP details the steps from beginning to end of the DMA data collection process. It is the process I used for all scaffold testing, and is specific to the Whittington Lab's 3D printed IsoTruss, Voronoi, and Truncated Octahedron Scaffolds.

Scaffold Testing SOP
Prepared by Elizabeth Hunt
June 2023

Preparing PBS Solution

1. Prepare 3 L of 1x concentrated phosphate-buffered saline (PBS) solution for the water bath:
    a. Prepare 10x concentrated PBS solution: add contents of PBS packet and DI water to 1 L of beaker, mix on stir plate until all of the particles have dissolved
    b. Fill 1 L bottle with 900 mL of deionized (DI) water
    c. Measure 100 mL of 10x concentrated PBS solution in a graduated cylinder and pour into the 1 L bottle with the DI water
    d. Storing extra:
        - Store extra solution in the fridge after clearly labeling the capped bottle with the contents, date, and your name
    e. Using stored solution that has been stored:
        - If there are any crystals that have formed after refrigeration, heat and stir on a stir plate until dissolved
        - Prepare solution using same steps as above

Setting Up Water Bath

1. The compression platen and submersible 22N load cell must be removed from the lower extension shaft before placing water bath onto the crosshead and the crosshead should be lowered to allow for enough room to place the water bath through the gap

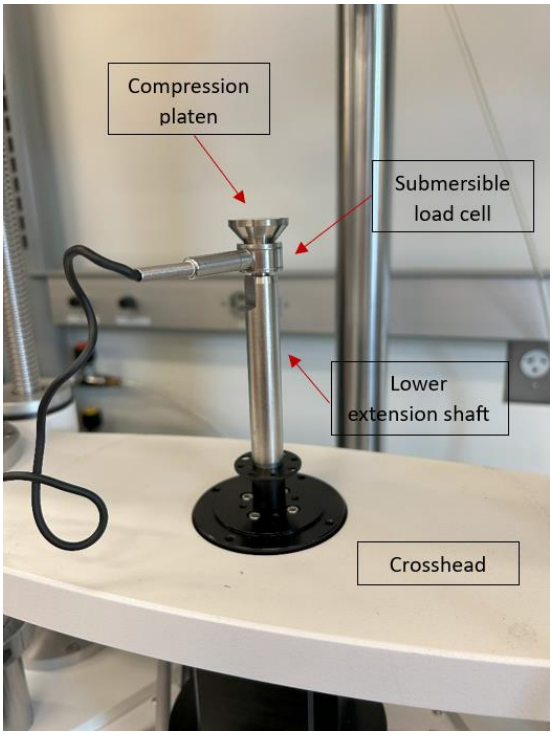

2. The hole on the bottom of the water bath must be aligned with the lower extension shaft by coming through the back of the machine (to avoid tangling the heating cords)
3. Lower the bath on top of the lower extension shaft until it rests on top of the crosshead with the draining spout facing forward as seen in the figure below

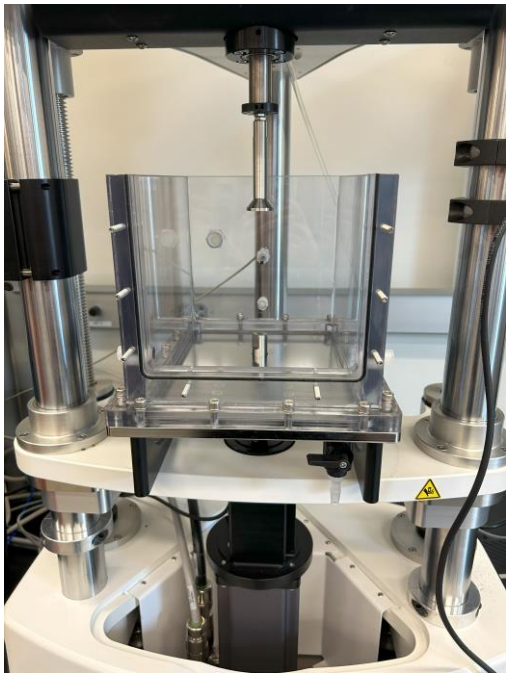

4. Screw in the four screws to fasten the mounting clamps around the lower crosshead on each side of the water bath
5. Screw the submersible 22N load cell onto the lower extension shaft and then screw the compression platen on top of the load cell
6. Replace the front cover onto the water bath, aligning the 8 screws and tightening firmly so that water does not leak out, but not too tight to strip the screws
7. Insert the temperature probe into the top center hole as shown in the figure below

8. Once everything on the water bath has been fastened and tightened so that no liquid can leak out, the solution can be poured into the top of the water bath
9. All 3 L of the solution already prepared should be poured into the water bath so that both platens and the temperature probe are submerged
10. The lower crossbar can be raised so that the top platen is submerged and there is about a 15 mm gap between the top and bottom compression platens

Heating Solution in Water Bath and Setting Up Sample

1. If not already powered on, flip on each of the switches on the power boxes to the left of the machine and open up WinTest on the desktop
    - Click enter when the “Login to WinTest” box pops up asking for a username and password
2. To open 22N load cell project file: File > Open Unsecure Workspace > Project… > 20-068_22N.prj
3. At the far right of the Test Setup window, select the DMA button under Applications – this will open up the DMA window where testing will be done

    - Again, click enter when the “Login to DMA” window pops up asking for a username and password
4. To open up the organoid project file: File > Open > organoid_DMA_training.tst
5. Unless the ElectroForce has been used for a different test, the compliance compensation should be complete already (if not, see DMA Setup SOP)
6. In the Specimen Insertion window, select the “Temp” radio button under Ramp to and enter 37 C in the window (shown in figure below)
    - If “Temp” is not an option, make sure that “Include Temperature Control” is checked in the Waveform Setup box
7. To begin heating the water, hit the Ramp to 37C button
    - To check that it is heating properly, go back to the WinTest window and the temperature window should be increasing and the Temp cmd window should read 37 C
    - This process takes a long time (about 30 to 45 minutes?)
    - Make sure that the water bath covers are on top of the bath to keep heat in

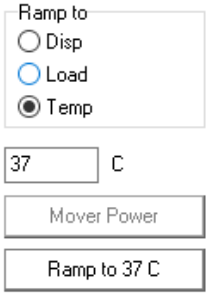

8. Once the temperature reaches about 36 C, drop the scaffold that will be tested first into the water bath to bring it to temperature
9. Once the temperature reaches 37 C, use gloves and the long forceps to place the scaffold so that it is centered on the top platen (it should float, so it’ll be positioned along the top platen; however, if it does not float position it on the bottom platen)
10. Zero the load by hitting the “Tare Load Channel” button in the Specimen Insertion window on the DMA setup screen
    - This should make it so that in compression, the 22N load cell window reads a negative force – that is okay
11. Come into contact with the sample by selecting the Load radio button under the Ramp to in the Specimen Insertion window, and enter -0.10 N in the box like in the figure below

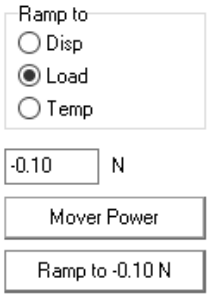

12. Ensure that Mover Power is on (if power is on, the Mover Power button will be green, if it is not green, push the button to turn power on)
13. Select the “Ramp to -0.10 N” button to come into contact with the specimen
14. Visually check the specimen to make sure it is in contact with both platens and centered on the platforms
15. Enter the Specimen ID that is currently inserted in the Specimen ID box at the bottom left of the DMA Window

Running Tests

1. Now that the solution is heated to body temperature and the scaffold is inserted properly, the first test is ready to begin
2. Open the first condition file by selecting the “Open Condition File” button at the bottom right of the DMA Window
3. Select the file called “Bone_Organoid_5_31_22N_Freq_Sweep.cyc
4. The inputs should not need to be adjusted, and should read as follows in the figure below

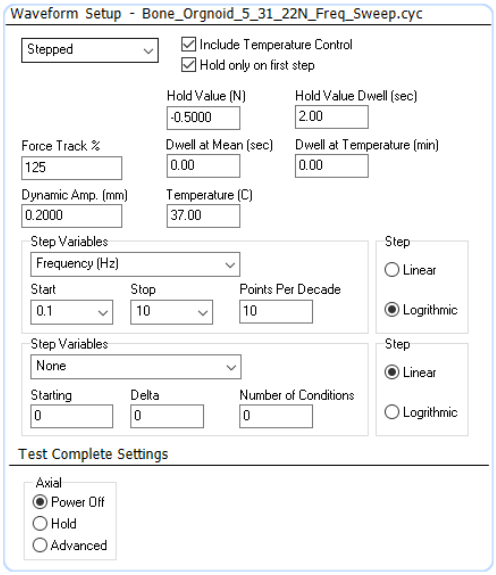

5. Select the “Next” button at the bottom right, and this window will pop up:

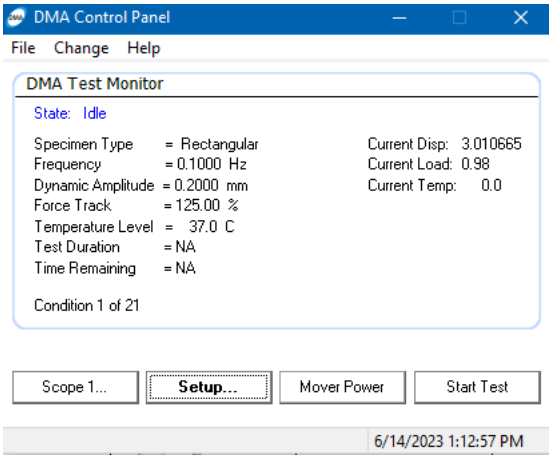

6. For this test, the frequency sweep, there will be 21 conditions and as the test progresses, the condition that is currently being tested will display as “Condition x of 21”
7. If the “Mover Power” button is not green, hit the button to turn the power on
8. Hit the “Start Test” button to begin testing
9. After the first condition is complete, a Trios window will open and begin to display the data as the test progresses
10. Once the test is over, the Trios window with the data can be closed, but make sure to save the data under a clear name that describes the test and which specimen is being tested
11. Return to the DMA Test Setup window by selecting the “Setup…” button
12. Before starting the next test, place next specimen into the heated solution to bring to temp
13. Perform the second test, the Strain Sweep, by opening Condition File called “Bone_Organoid_5_31_22N_Strain_Sweep.cyc” the same way the frequency sweep file was opened
14. Again, nothing should need changing, and the test inputs should look like the following:

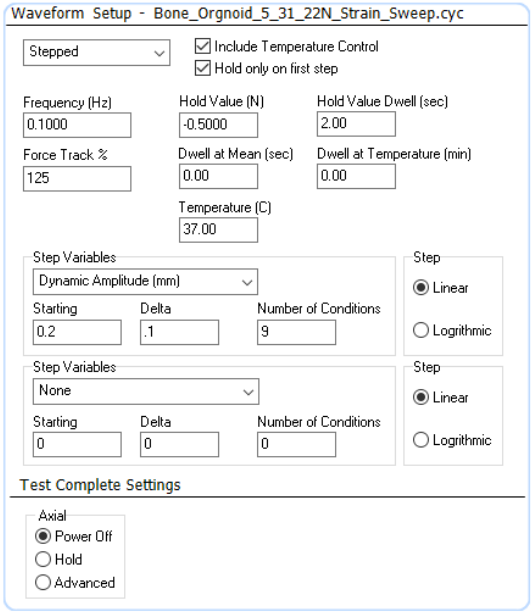

15. Repeat steps 5 through 10 with the Strain Sweep test file – as shown in the figure below, there are 9 conditions for the Strain Sweep

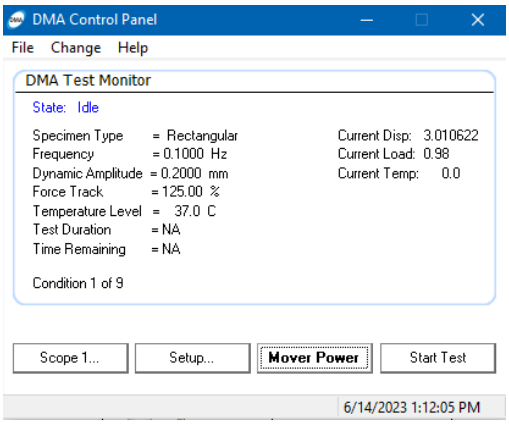

16. Repeat these steps to load and test the scaffolds until all have been tested, placing completed scaffolds back into the well it came from

Cleaning

1. All cleaning should be done wearing proper PPE (gloves, lab coat, goggles)
2. After unloading the last scaffold, the well plate should be closed, labeled clearly, and put in the refrigerator
3. Drain the solution with the spout by releasing the solution into a container larger than 3 L
    - Hold the container the whole time the water bath is draining to prevent spills
4. Dump the solution in the sink
5. If there is still some solution left in the water bath, wipe as much as you can up with paper towels before lifting the water bath off of the lower extension shaft
    - It will probably help to unscrew the front screws and take off the front window to help with cleaning and taking off the water bath
6. Unscrew the compression platen and submersible load cell and spray with 70% ethanol and set to dry on a paper towel
    - Be careful not to damage the load cell with excessive pressure
7. Lift the water bath off the extension shaft and bring behind the machine and around to the left of the power boxes to be cleaned
8. Spray the metal extension shafts and top compression platen with 70% ethanol and wipe down
9. Wipe the water bath down with soapy water and rinse with DI water being careful not to get the heating cords and plates wet
10. Lay it upside down to dry on a paper towel
11. Any metal materials that have been used should be rinsed with DI water then wiped down with 70% ethanol and either air dry on the rack above the sink or on a paper towel
12. Any surfaces that were worked on should be wiped down with 70% ethanol